

Alma Mater Studiorum Università di Bologna
Archivio istituzionale della ricerca

Iron-based electrocatalysts derived from scrap tires for oxygen reduction reaction: Evolution of synthesis-structure-performance relationship in acidic, neutral and alkaline media

This is the final peer-reviewed author's accepted manuscript (postprint) of the following publication:

Published Version:

Muhyuddin, M., Testa, D., Lorenzi, R., Vanacore, G.M., Poli, F., Soavi, F., et al. (2022). Iron-based electrocatalysts derived from scrap tires for oxygen reduction reaction: Evolution of synthesis-structure-performance relationship in acidic, neutral and alkaline media. ELECTROCHIMICA ACTA, 433, 141254-1-141254-13 [10.1016/j.electacta.2022.141254].

Availability:

This version is available at: <https://hdl.handle.net/11585/900818> since: 2022-11-08

Published:

DOI: <http://doi.org/10.1016/j.electacta.2022.141254>

Terms of use:

Some rights reserved. The terms and conditions for the reuse of this version of the manuscript are specified in the publishing policy. For all terms of use and more information see the publisher's website.

This item was downloaded from IRIS Università di Bologna (<https://cris.unibo.it/>).
When citing, please refer to the published version.

(Article begins on next page)

This is the final peer-reviewed accepted manuscript of:

Muhyuddin, M., Testa, D., Lorenzi, R., Vanacore, G. M., Poli, F., Soavi, F., Specchia, S., Giurlani, W., Innocenti, M., Rosi, L., Santoro, C., Iron-based electrocatalysts derived from scrap tires for oxygen reduction reaction: Evolution of synthesis-structure-performance relationship in acidic, neutral and alkaline media. 2022, Electrochimica Acta, 433, 141254

The final published version is available online at:

<https://doi.org/10.1016/j.electacta.2022.141254>

Terms of use:

Some rights reserved. The terms and conditions for the reuse of this version of the manuscript are specified in the publishing policy. For all terms of use and more information see the publisher's website.

This item was downloaded from IRIS Università di Bologna (<https://cris.unibo.it/>)

When citing, please refer to the published version.

Iron-based Electrocatalysts Derived from Scrap Tires for Oxygen Reduction Reaction: Evolution of Synthesis-Structure-Performance Relationship in Acidic, Neutral and Alkaline Media

Mohsin Muhyuddin¹, Davide Testa¹, Roberto Lorenzi¹, Giovanni Maria Vanacore¹, Federico Poli², Francesca Soavi², Stefania Specchia³, Walter Giurlani⁴, Massimo Innocenti⁴, Luca Rosi⁴, Carlo Santoro^{*1}

¹Department of Material Science, University of Milan Bicocca, U5 Via Cozzi 55, 20125, Milan Italy

² Department of Chemistry “Giacomo Ciamician”, Alma Mater Studiorum University of Bologna, Via Selmi 2, 40100 Bologna, Ital

³ Department of Applied Science and Technology, Politecnico di Torino, Corso Duca degli Abruzzi 24, Torino 10129, Italy

⁴ Università degli Studi di Firenze, Polo Scientifico e Tecnologico di Sesto Fiorentino, Via della Lastruccia, 3, 50019 Sesto Fiorentino FI, Italy

***Corresponding author:** Carlo Santoro. E-mail: carlo.santoro@unimib.it

Abstract

Mass generation of scrap tires presents a major challenge for environmental safety, however, their upcycling into carbon-based nanomaterials by the virtue of pyrolysis treatments can open up new windows for energy conversion and storage technologies in the context of the circular economy. Herein, we report the synthesis of Fe-N-C oxygen reduction reaction (ORR) electrocatalyst for fuel cell (FC) applications using carbonaceous char derived from scrap tires through microwave-assisted pyrolysis (MAP). The char obtained from MAP was activated with potassium hydroxide and then pyrolyzed at a high temperature to fabricate Fe-N-C after mixing with iron and nitrogen precursors. Finally, the developed Fe-N-C was ball-milled and acid-etched for homogenization and leaching of iron oxide nanoparticles. In this study, structural evaluation during each synthesis step was elucidated and correlated with the ORR activity in all three pHs i.e. acidic, neutral, and alkaline. Moreover, the effect of electrocatalyst loading on ORR kinetics was also analyzed using two different loadings (0.2 and 0.6 mg cm⁻²) on the rotating ring disk electrode (RRDE). The developed Fe-N-C demonstrated encouraging onset potentials of 0.881, 0.822, and

0.936 V vs RHE in acidic, neutral, and alkaline conditions, respectively. Whereas the ORR activity was slightly reduced after the milling-etching step. Lower peroxide yield together with a tetra-electronic reduction of oxygen was witnessed in acidic and neutral conditions, however, peroxide production was increased in the alkaline medium.

Keywords: scrap tires, oxygen reduction reaction, PGM-free electrocatalysts, electrocatalytic activity

1. Introduction

Safe disposal of scrap tires has become a worldwide persistent challenge where a major proportion of discarded tires is tossed out without any treatment. By the year 2030, global scrap tire generation is expected to exceed 1.2 billion tires per annum [1–3], while approximately 5 billion tires are already amassed [3,4] which eventually will enter into the waste streams, signifying a severe threat to the ecosystem. Traditional waste management pathways such as landfilling or energy recovery via incineration of tires not only contribute to the planetary carbon footprint but also become the cause of toxicity (air, water, and soil) and human health hazards [4,5]. In such a scenario, the theme of the circular economy becomes more relevant representing the safest recovery and valorization of waste products [6] which could be primarily important for scrap tires [7].

Tires are typically made up of synthetic and natural rubbers, carbon black, metallic substitutions, fabrics and other additives i.e. sulfur, pigments, ZnO, silica, etc., hence constituting nearly 74-76% carbon in their total composition [1,8]. Therefore, scrap tires can be effectively valorized into carbon-based nanomaterials that could find their potential applications in electrochemical energy conversion & storage technologies which are the key focus of contemporary research amid the foreseen extinction of fossil fuels and manmade global warming [7,9–11]. Chars derived from different biomass and plastics have been produced and tested in electrochemical devices. In parallel, carbons derived from scrap tires can also be produced with enhanced economic viability compared to other sources [11,12].

Among the various energy conversion technologies, fuel cells (FCs) have captured scientific recognition owing to their extraordinary advantages, especially very high conversion efficiencies, portability, no emission of greenhouse gases, and the ability to operate at a lower

temperature range [13–15]. Such benefits can effectually relieve the existing contradiction between environmental safety and proliferated energy demands by replacing or supporting battery-powered electric automobiles with fuel cell vehicles (FCVs). However, despite the deep scientific interest, considerable commercial deployment of FCs is still far from reality and principally obstructed due to the utilization of platinum group metal (PGM) electrocatalysts which are used to overcome the sluggish oxygen reduction reaction (ORR) at the cathodic side of the device. In fact, to improve the kinetics of ORR electrocatalysis, highly expensive and scarce PGMs are used, accounting for ~30% of the total cost of a configured device [16]. Moreover, Pt-based electrocatalysts are prone to degrade with methanol and have low stability against carbon monoxide [15]. Therefore, the development of a cost-effective and efficient electrocatalyst without having the aforesaid demerits is a critical bottleneck to rationalizing the FC application. At this juncture, first-row earth-abundant transition-metal (TM) nitrogen carbons also named TM-N-Cs (with TM as Mn, Fe, Co, Ni, Cu) are promising alternative PGM-free electrocatalysts in which TM-N_x active moieties dispersed in the carbon framework can uplift the ORR activity, especially in neutral and alkaline electrolytes [17]. The structural attributes of TM-N-C demonstrate an encouraging potential to replace Pt due to the high electrocatalytic activity and predominance of tetra-electronic selectivity towards ORR [18]. In TM-N-C, carbon being matrix not only provides fundamental support for the electrocatalytically active moieties but also vigorously participates in determining the overall ORR activity. Such carbon-based support can be competitively derived from the pyrolysis of waste biomasses and waste plastics, producing sustainable char [19–22]. Recently, various polymeric waste products such as polypropylene [23], polyurethane [24], polyvinyl-butyril [25], low-density polyethylene [26], polyethylene terephthalate [27], surgical face masks [28], etc. have been valorized into PGM-free electrocatalysts in the pursuit of ecological recycling of the plastic waste within the core of the circular economy.

In addition to typical waste plastics, upcycling the scrap tires into carbon-based PGM-free electrocatalysts can simultaneously address both leading problems of today's world related to environmental pollution and clean energy production. Very recently, a few examples have been reported transforming scrap tires into nanomaterials for electrocatalysis with interesting properties. Hood et al. synthesize the carbon support for Pt-carrying ORR electrocatalysts from waste tire rubbers [11]. In 2019, Passaponti and coworkers formulated a strategy to upcycle scrap tires into PGM-free electrocatalysts by adopting a simplistic route of microwave-assisted pyrolysis (MAP),

where the post-pyrolysis annealing condition remarkably influenced the overall performance of the derived electrocatalysts in alkaline media [29]. In a separate investigation, the ORR performance of the MAP-derived char was further enhanced through an electrochemical enrichment with cobalt and a positive shift of 40 mV relative to pristine char was witnessed [30]. Veksha et al. reported the synthesis of carbon nanosheets with heterogeneous doping of sulfur, nitrogen, and oxygen for ORR applications through catalytic-chemical vapor deposition employing the scrap tires as an initial precursor [31]. Very recently, Kang et al. developed nitrogen-doped metal-free electrocatalysts from sulfonated scrap tires which demonstrated an encouraging onset potential of 0.89 V vs RHE with nearly tetra-electronic electro-reduction of oxygen in 0.1 M KOH [32].

Although the recent advances of the past 2-3 years outline a motivation for the development of polymeric waste-derived ORR electrocatalysts, novel routes to further valorize polymeric waste specifically from scrap tires can be properly designed and finally pursued. In fact, during the electrocatalyst synthesis, different TM and nitrogen-based active moieties are produced in the carbon's framework, for instance, nitrogen-containing species (oxygenated, graphitic, pyrrolic and pyridinic), TM-N_x sites (x = 2, 3, 4) and encapsulated TM nanoparticles in the form of oxides, carbide, nitride and so on are produced [33]. The scientific community has agreed on the point that a large amount of homogeneously dispersed and easily accessible TM-N_x moieties within the carbonaceous architecture are the definite active sites for the desirable tetra-electronic reduction of oxygen [34]. Moreover, the pyridinic-N is suspected to have the capacity of catalyzing the subsequent reduction of peroxide species into H₂O, recovering the overall improved efficiency of the system [35]. The role of electrochemically active moieties is often correlated to the fact that the micropores act as nucleation sites for the accessible moieties [36]. Such an uncertain situation also prevails in the waste-derived PGM-free electrocatalysts where the role of the synthesis route on the development of active sites, transport mechanism of gases within the carbon support, accessibility of active centers, electronic conductivity, and the effects of morphological parameters also must be addressed in detail. It was shown that the steps involved in the synthesis process such as the use of sacrificial support, chemical activation, ball milling, the selection of the precursors, first, or second pyrolysis and acid washing predominantly affect the physicochemical properties of achieved electrocatalyst [24,37–40]. Consequently, it becomes important to launch a systemic study to thoroughly analyze the effect of the synthesis route on the overall catalytic ability and

selectivity towards the tetra-electronic ORR. In addition to this, the different active sites can be protonated and/or deprotonated depending on the operating pH, behaving differently in acid, neutral and alkaline electrolytic conditions. Hence, operating conditions at different pHs lead to different electron transfer mechanism pathways offering distinct advantages. When the pH of the electrolyte is changed, the physiochemical characteristics of the active centers are also changed, in turn, the overall reaction pathway and kinetics are modified [41].

Based on the above considerations, herein we report a systematic study to develop a novel Fe-N-C electrocatalyst utilizing scrap tires as a valuable precursor. The experimental design comprises of 1) microwave-assisted pyrolysis, 2) activation using potassium hydroxide, 3) functionalization with TM and N during the high-temperature pyrolysis, and 4) ball milling and acid etching. This work aims to correlate the structural evolution of derived electrocatalysts with the electrochemical performance in a wide range of pH. Therefore, advanced characterization techniques and spectroscopic tools were combined to identify the impact of the structure and morphology of Fe-N-C on its electrocatalytic activity in three different media: acidic (0.5 M sulfuric acid, H_2SO_4), neutral (0.1 M phosphate buffer solution, PBS) and alkaline (0.1 M potassium hydroxide, KOH).

2. Experimental Methods

The objective of the presented study was to identify relationships among the synthesis, structure, and performance of the PGM-free electrocatalysts derived from scrap tires. This was important to understand the changes caused by each synthesis step to improve the synthesis methodology. Therefore, a comprehensive experimental design involving several steps was adopted to closely monitor the effect of processing on the structure achieved and hence its ultimate influence on the ORR performance. The overall experimental route followed is schematized in Figure 1, whereas the inclusive description of each step can be found in the upcoming subsections.

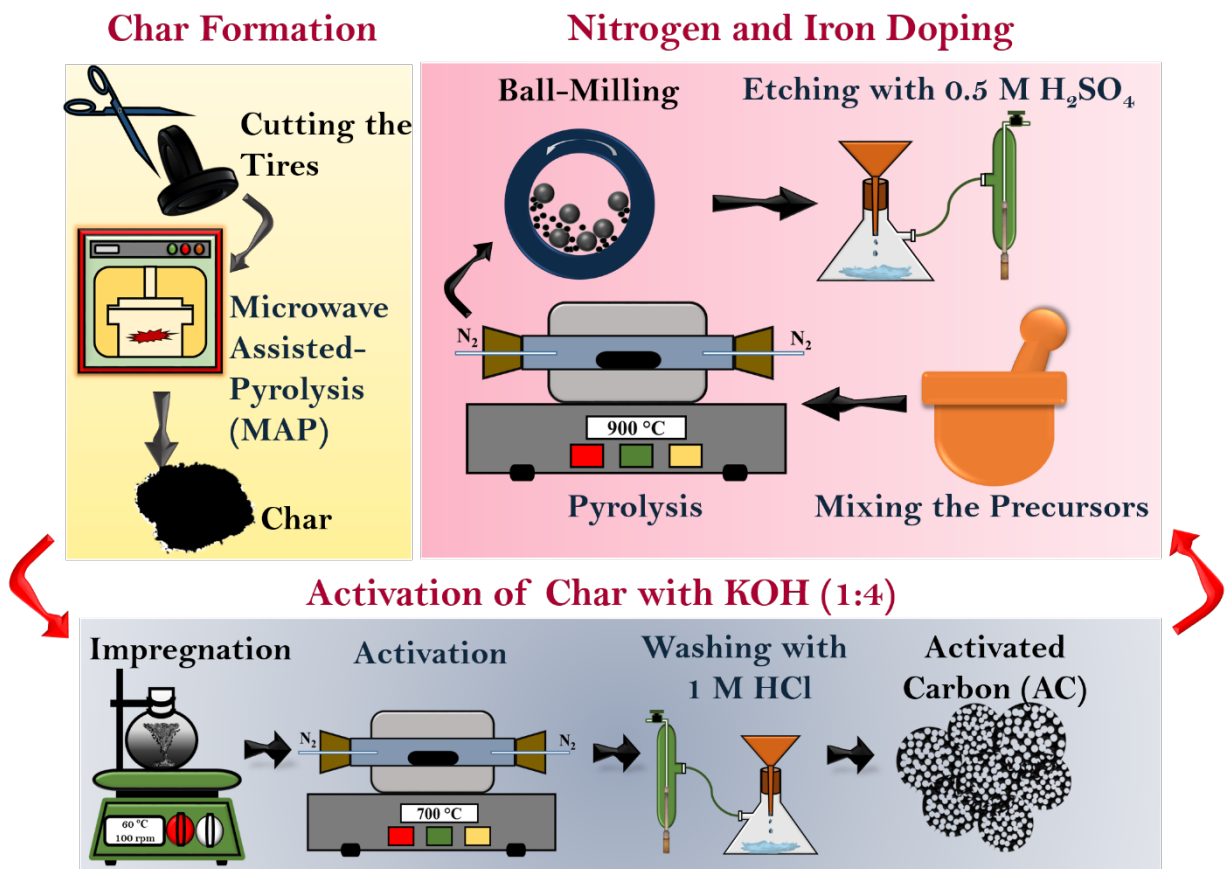


Figure 1. Demonstration of experimental research design for the transformation of scrap tires into Fe-N-C electrocatalyst

2.1 Transformation of scrap tires into carbonaceous char

In the synthesis of Fe-N-C electrocatalysts, the first step was to acquire char from commercial waste tires through MAP by reproducing a previously reported method [29]. Briefly, an automobile tire (Michelin model Agilis 81–195/65 R16C) was cut into tiny chips followed by drying at 65 °C. The tire sample used in the study was isolated from metal wires/reinforcement and majorly consisted of carbonaceous matter [29,42]. Fully dried chips were then subjected to a microwave (MW) oven working at 1200 MW power for 37 min in a nitrogen atmosphere while keeping the specific power of the pyrolyzing system at 24 kW kg⁻¹. The char acquired was labeled as ‘C’.

2.2 Activation with KOH

In addition to optimizing the dispersion of the electrochemically active sites and their accessibility, a well-dispersed porosity is fundamentally important for ORR activity. Macropores serve as ion buffering reservoirs, mesopores ensure fast transportation of ions and oxygen and accessibility to the active centers whereas the micropores accommodate the charges in the electrical double layer [15,24]. The sacrificial support method involving silica is used as a hard templating method to create regular and uniform pores [38,43–48]. However, for template removal, the usage of harsh acids i.e. HF is the biggest disadvantage of this practice. In parallel, chemical activation through KOH becomes a simplistic and highly effective strategy to promote the surface area in the carbon support [7,40,49]. To produce activated carbon (AC), C derived from MAP was impregnated with KOH in a weight ratio of 1:4 (Carbon: KOH) in absolute ethanol (Merck) for 12 h and the mixture was subsequently dried in a nitrogen environment at 60 °C while stirring continuously [49]. Afterwards, the slurry obtained was subjected to heat treatment at 700 °C for 1 h in flowing pure nitrogen ($100\text{ cm}^3\text{ min}^{-1}$) with heating and cooling ramp rates of $5\text{ }^{\circ}\text{C min}^{-1}$. Heat treatment was done in a quartz tube furnace (Carbolite). To avoid any reaction between quartz and KOH, a sheet of stainless steel (0.1 mm, PI-KEM) was inserted inside the tube, covering the internal wall of the quartz tube. After heat treatment, the resultant was then washed three times using a solution of 1 M HCl and plenty of milli-Q water until the neutral pH of the supernatant was achieved [49]. Finally, the AC was dried overnight in a vacuum oven at 80°C to remove the remaining moisture.

2.3 Synthesis of Fe-N-Cs derived electrocatalysts from MAP scrap tires

The AC achieved in the second step was doped with iron and nitrogen by mixing it with an iron salt and nitrogen-containing organic molecules. Particularly, 5 wt% iron nitrate nonahydrate (Alfa Aesar) and 15 wt% 1,10-phenanthroline (Sigma Aldrich) were homogeneously mixed with AC (80 wt%) followed by pyrolysis at 900 °C for 1 h in nitrogen atmosphere ($100\text{ cm}^3\text{ min}^{-1}$) with heating and cooling ramp rates of $5\text{ }^{\circ}\text{C min}^{-1}$. The resulting material was named ‘ACP’. In the next phase, the cooled ACP was thoroughly ground by using a high-energy ball miller (E_{MAX}, Retsch GmbH, Germany) with zirconia balls of 3 mm diameter at 400 rpm for 2 h with 5 min rest after every 30 min. In the fourth stage, ball-milled ACP was etched with boiling 0.5 M H₂SO₄ for 15 min to etch out the oxides and Fe nanoparticles. After etching with acid, the material was washed with a copious amount of milli-Q water (until neutral pH was achieved) and dried over the night

in a vacuum oven at 80 °C and the sample taken at this stage was named as ‘ACPE’. The nomenclature of the samples synthesized and tested in this study is presented in Table 1 along with the description of the experimental step at which they were recovered.

Table 1. Designation of samples abbreviations used in this study

S. No.	MAP	KOH- Activation	Pyrolysis (at 900 °C)	Ball Milling	Acid Etching	Sample Abbrev.
1	x					C
2	x	x				AC
3	x	x	x			ACP
4	x	x	x	x	x	ACPE

2.4 Electrochemical Measurements

The electrochemical performances of the synthesized electrocatalysts were evaluated using the rotating ring disk electrode (RRDE) technique (Pine WaveVortex RDE assembled with a Pine bipotentiostat). To prepare ink, 5 mg of as-developed electrocatalyst was mixed with 985 µL of isopropanol (Alfa Aesar) after which 15 µL of 5 wt.% Nafion® D-520 (Alfa Aesar) was added to the dispersion. The produced inks were probe sonicated for 10 min at 50 % pulse amplitude. Afterwards, the ink-containing vials were placed in an ultrasonic bath for 30 min at room temperature. The RRDE (E6R2 series) used in the electrochemical study had a disk area of 0.2376 cm² with a Pt ring of 0.2356 cm² geometric area, while the collection efficiency (N) was 38%. The working electrode was fabricated by drop-casting using a precision pipette and left for drying at room temperature. In this study, two different loadings of electrocatalysts were analyzed: 0.2 and 0.6 mg cm⁻². For making a comparison with the benchmark Pt electrocatalyst, commercially available 20 wt.% Pt supported on carbon (Pt/C) was used as a standard material while keeping its loading on RRDE as 30 µgPt cm⁻² [50,51].

The experiments were carried out in three different electrolytes: i) acidic solution of 0.5 M H₂SO₄; ii) neutral solution of 0.1 M potassium phosphate buffer (PBS) [52]; iii) alkaline solution of 0.1 M KOH. Linear sweep voltammetry (LSV) was performed using a three-electrode configuration comprising of RRDE as a working electrode, Pt wire as a counter electrode and saturated calomel electrode (SCE) as a reference. The potential window for acidic, neutral, and

alkaline electrolytes was maintained at +1000 to -250 mV vs SCE, +600 to -750 mV vs SCE and +150 to -1050 mV vs SCE, respectively. The rotation speed for all the experimentation was kept at 1600 rpm, while the ring potential was always kept at 1200 mV vs RHE (reversible hydrogen potential). The ORR experimentation also involved the bubbling of pure oxygen inside the electrolytic solution at least 30 min before and during the RRDE experiments to ensure a sufficient level of oxygen saturation. Before actual measurements, all the electrocatalysts were first activated in electrolytes by performing CV cycles at 100 mV s⁻¹ until a steady trend in the current is achieved and finally the LSVs were acquired at the scan rate of 5 mV s⁻¹. By monitoring the disk current (I_{disk}) and ring current (I_{ring}), peroxide formation (eq.1) and electron transfer number (n, eq.2) were calculated using the following equations:

$$Peroxide (\%) = \frac{200 \times \frac{I_{ring}}{N}}{I_{disk} + \frac{I_{ring}}{N}} \quad (eq.1)$$

$$n = \frac{4 I_{disk}}{I_{disk} + \frac{I_{ring}}{N}} \quad (eq.2)$$

As a final point, all the potential values were converted into potential versus RHE using the following relationship (eq.3):

$$E(vs\ RHE) = E(vs\ SCE) + E^{\circ}_{SCE} + (0.0591 \times pH) \quad (eq.3)$$

Where E°_{SCE} is equal to 0.241 V.

To assess the operational durability of the best-performing electrocatalyst short-term stability test was carried out in each electrolyte over 2500 cycles at 50 mV s⁻¹. The working electrode was prepared with 0.6 mg cm⁻² loading on RRDE and after every 500 cycles, LSV was acquired at the scan rate of 5 mV s⁻¹.

2.5 Chemical and Morphological Characterizations

The thermal response of the samples was evaluated using thermo-gravimetric analysis (TGA) coupled with differential scanning calorimetry (DSC1) in the STARe system, (Mettler Toledo TOLRDO). TGA was conducted by heating the adequate quantity of samples from 30 °C to 950 °C in a nitrogen environment with a ramp rate of 10 °C min⁻¹. Crystallographic investigations were carried out through X-rays diffraction (XRD) of powdered samples with Rigaku Miniflex 600 in a 2θ range between 10° and 80°. The morphological and elemental

investigations were performed via transmission electron microscopy (TEM) using a JEOL JEM 2100P operating at 200 kV, equipped with a Gatan RIO CMOS camera for high-resolution imaging (nominal point resolution of 2.4 Å), an Oxford Energy Dispersive X-Ray (EDX) detector, and Bright-Field (BF) and High Angle Annular Dark-Field (HAADF) Scanning TEM (STEM) detectors. The samples undergo preparation before the measurements. Particularly, the synthesized samples were diluted in a solvent solution and transferred via drop-casting onto a Cu grid covered by a thin (3-4 nm) amorphous carbon membrane.

The Raman spectrometer (LabRam, Jobin Yvon, France) connected with BX40 microscope (Olympus, Japan) having a Long Working Distance 50x objective (N. A.: 0.60) was utilized for focusing helium-neon laser with an excitation wavelength of 632.8 nm. Raman signals were collected in backscattering configuration using a silicon CCD (Sincerity, Jobin Yvon, France) operating at 200 K. All the obtained spectra were normalized to the peak intensity of the *G* band after subtraction of baseline. Jasco FT/IR-4100 (Fourier-transform infrared) spectrometer assembled with attenuated total reflectance (ATR) was used to investigate the surface chemistry of powdered electrocatalysts. The FTIR experimental data were normalized and studied using Spectra Manager™ Suite software. FTIR samples were prepared by mixing 1 mg of as-developed electrocatalyst with 100 mg of KBr. The measurements in transmittance mode were obtained in the range of 4000 to 570 cm⁻¹ with 64 accumulations at 4.0 cm⁻¹ resolution. CHNS elemental analysis was carried out using an Elementar Vario Microcube Device by setting the combustion tube and oxidation tube at 1100°C and 850°C, respectively.

X-ray photoelectron spectroscopy (XPS) was performed to determine the elemental surface composition of the four samples. The analysis was carried out using a Physical Electronics PHI 5000 Versa Probe electron spectrometer system with a monochromatic Al K α X-ray source (1486.60 eV) operated at 23.8 W, 15 kV and 1 mA anode current. To reduce any possible charging effects of X-rays, a dual-beam charge neutralization method was applied, combining both low-energy ions and electrons. The samples were previously outgassed in an ultrahigh vacuum chamber at 2.5·10⁻⁶ Pa for 12 h. and calibrated against a value of the C 1s binding energy of 284.5 eV. Survey scans as well as narrow scans (high-resolution spectra) were recorded with a spot of 100 nm size. The survey spectra were collected from 0 to 1200 eV. The narrow C 1s spectra were collected from 278 to 302 eV, the narrow N 1s spectra from 390 to 410 eV, the narrow O 1s spectra from 522 to 544 eV, and the narrow Fe 2p spectra from 700 to 740 eV. All measurements were

affected by a standard deviation of about 0.4 eV. CasaXPS software was used for obtaining semi-quantitative atomic percentage compositions, using Gauss–Lorentz equations with a Shirley-type background. A 70 % Gaussian/30 % Lorentzian line shape was used to evaluate peaks position and areas.

The porosity of the samples was evaluated by nitrogen adsorption porosimetry measurements that were carried out at 77 K with an ASAP 2020 system (Micromeritics) after a drying step for 24 h at 413 K. The N₂ adsorption isotherms were analyzed by the Brunauer-Emmett-Teller (BET) and density functional (DFT) theories to obtain the specific surface area (S_{BET}) and pores size distribution (PSD), respectively.

3. Results and Discussion

3.1. Surface chemistry and morphology of the MAP-derived electrocatalysts

During the development of plastic waste-derived nanomaterials, the problem encountered at the first glance is a lower carbonaceous yield since a considerable mass is transformed into gaseous and oil-based products at higher temperatures. In this study, scrap tires were used as a carbon precursor and were transformed into carbonaceous char through MAP as reported recently by Passaponti et al. [29]. KOH activation and high-temperature pyrolysis were adopted in the synthesis expedition. Therefore, TGA was employed to simulate the thermal profile of raw ingredients during these processes and the observed trends are illustrated in Figure S1. It is noteworthy that ‘C’ showed only ~5.5 wt% mass loss till 950 °C. Hence, the TGA profile determined that any temperature within the limits of pyrolysis can be adopted without sacrificing a considerable amount of carbon. When the sludge containing C-impregnated with KOH (1:4) was subjected to TGA (inset of Figure S1a) an initial weight loss of ~35 wt% till 200 °C followed by an isotherm till 800 °C was shown. In C impregnated with KOH, another decrease in weight can be witnessed at a temperature higher than ~800 °C which might be due to the decomposition of K₂CO₃ (supposed to form at 400 °C during the activation reaction profile) [25]. However, in the case of KOH activation, thermal treatment was carried out at 700 °C. A thermal trend similar to that of C was tracked by a pyrolyzing mixture of ACP (Figure S1b). However, a sharp weight loss nearly at 200 and 320 °C might be attributed to thermal degradation of iron nitrate and 1,10-phenanthroline, respectively, as depicted by pure precursors in the inset of Figure S1b. Moreover, the solid carbonaceous yield of the sample achieved at each experimental step is presented in Table

S1. With the aim of the crystallographic investigation and phase identification, all the as-developed samples were analyzed through XRD and the achieved diffraction patterns in the 2θ range of 10° to 80° are displayed in Figure 2a. Diffraction peaks of graphitic carbon are identified in every sample at $\sim 25^\circ$ and $\sim 44^\circ$ corresponding to (002) and (100) lattices, respectively [53]. However, with respect to sample C, all the samples showed a negative shift of the (002) plane towards lower 2θ , representing an increase in lattice parameters which was most prominent in the case of AC. Lv et al. have previously explained the enhancement of lattice parameters accompanied by an overall expansion of the carbon framework due to the etching of KOH on the walls of mesopores during the activation process [49]. Pristine sample 'C' also showed diffraction peaks of ZnS as a major impurity phase. The peaks that emerged at 28.72° , 33° , 47.6° , 56.36° , and 76.8° were consistent with JCPDS# 00-005-0566 of cubic ZnS and can be assigned to diffracting lattices of (111), (200), (220), (311) and (331), respectively. Interestingly, all the ZnS peaks disappeared during KOH activation, demonstrating a bi-efficacious effect of this step. It should be pointed out that the functionalization of AC with Fe and N during the high-temperature pyrolysis (sample ACP) gave rise to the formation of Fe_3O_4 nanoparticles (matched with JCPDS# 00-003-0863). Fe_3O_4 exhibited six minor peaks at 30.1° , 35.72° , 43.18° , 53.9° , 57.09° , and 62.83° corresponding to (220), (311), (400), (422), (511) and (440), respectively [54,55]. However, magnetite nanoparticles were considerably etched out during the acid washing step (ACPE) and no peaks diffracting from the Fe species were observed, implying atomically dispersed iron in the carbon matrix most likely in Fe-N_x coordination.

Nanoscale morphology, structural arrangements, and elemental composition within the as-developed samples were analyzed using TEM and obtained micrographs are illustrated in Figure 2b-m. Images shown in Figure 2b-h were taken at room temperature at different magnifications with the TEM operated in bright-field parallel imaging mode and adopting an in-gap objective aperture. The pristine sample C directly derived from scrap tires through MAP exhibited agglomerated carbon particles with a large number of ZnS nanoparticles (Figure 2b-c). Nevertheless, KOH activation led to the destruction of graphitic regularity and the formation of highly porous amorphous networks. TEM micrographs of AC further confirm the removal of ZnS impurity phase during the activation step. It is worth noting that in Figure 2e nano-sized ripples were produced at the edges of wrinkled graphitic layers suggesting the development of micro/mesopores. On the other hand, after the pyrolysis of AC with iron and nitrogen precursors

at 900 °C, aggregates of Fe-based nanoparticles appeared. Figure 2f suggests the coexistence of graphitic and disordered carbon nanosheet-like structures in which iron oxide nanoparticles with a size range of 25-40 nm are embedded. Such nanoparticles encapsulated and wrapped between the few graphitic layers can be more precisely appreciated in Figure 2g-h (also in Figure S2). To categorically visualize the aggregation of Fe-based nanoparticles, BF-STEM, and elemental area map of the sample before acid etching are illustrated in Figure 2j-m. Besides the obvious accumulation of Fe at the nanoparticle, we observed a homogeneously dispersed nitrogen as well as iron within the main carbon matrix as derived by the elemental area mapping.

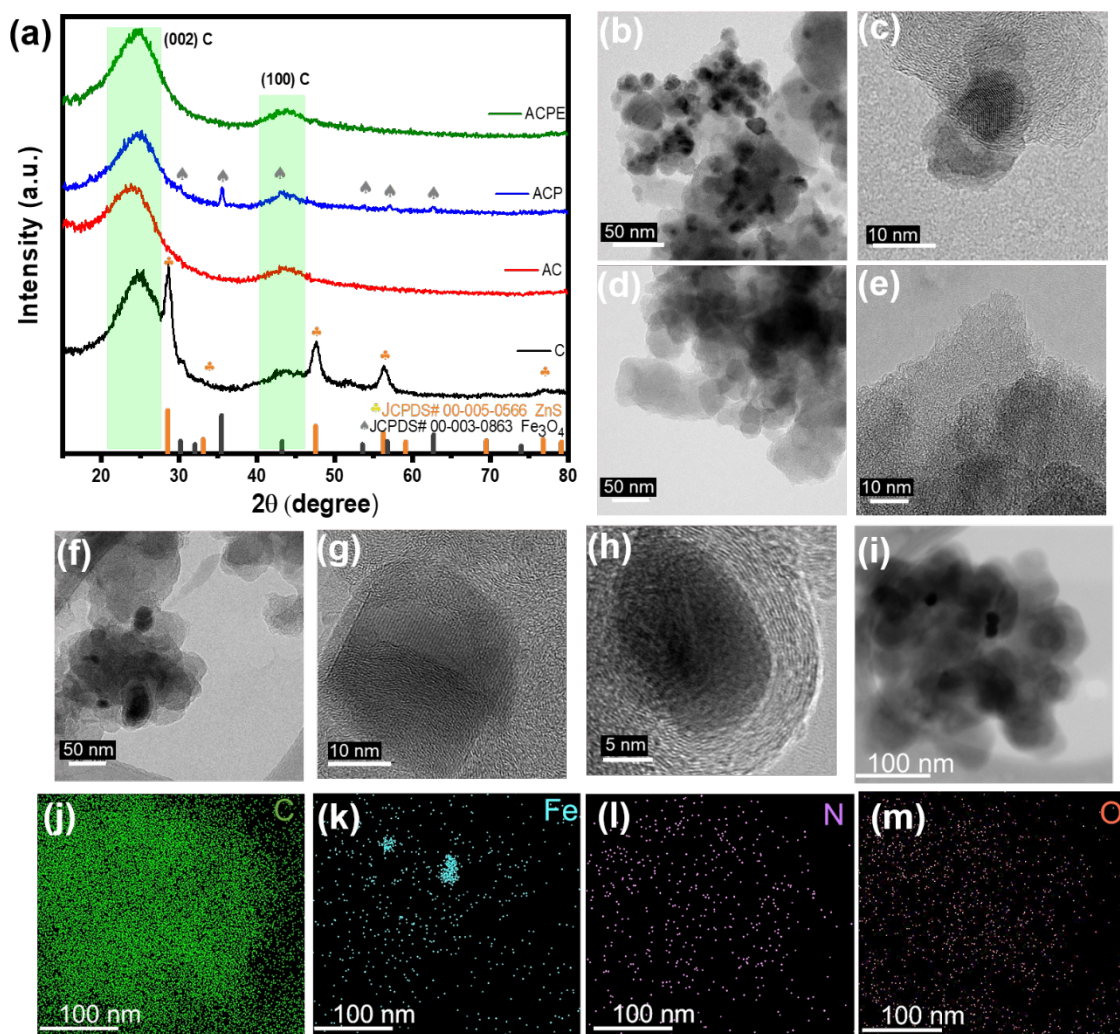


Figure 2. XRD patterns of all as-developed samples (a), TEM images of pristine C (b,c), AC (d,e), ACP (f-h), and BF-STEM (i) with corresponding elemental area map (j-m) of ACP showing distributed Fe, N, and O within the carbon matrix

Since the carbon matrix provides a governing platform for the electrochemically active centers to perform electrocatalytic reactions with appreciable kinetics, therefore, its integrity in terms of graphitization and distribution of intrinsic or induced defects is important to characterize. Raman spectroscopy is an essential tool that acts as a key supplement to XRD and TEM in the investigation of such carbonaceous nanomaterials. Graphitization in Fe-N-Cs might be helpful in electronic conductivity during electrocatalysis [56] but a large number of intrinsic defects such as corners, holes, broken fringes, zig-zag edges, etc. clearly improve the ORR activity by increasing the number of available active sites [57]. It is known in the community that defective edge carbons are crucial for electrocatalysis, as the edges and defects offer plentiful accessible absorption and reaction sites [57,58]. Raman spectra provided in Figure 3a highlight the predominance of the *D* and *G* bands at ~ 1330 and ~ 1586 cm^{-1} , respectively, in all the samples. *G* band is related to the translational motion of perfect sp^2 graphitic lattices with E_{2g} symmetry, whereas the *D* band emerges due to the presence of structural defects such as broken edges, disruption in graphitic structure, and sp^3 -like discontinuities. Hence, the I_D/I_G becomes a crucial indicator to define the degree of structural defects in carbon-based materials. Pristine sample ‘C’ showed a very intense *G* peak with I_D/I_G of 0.91. However, after activation, not only the intensity of *G* peaks was reduced but also the corresponding *D* peak broadened. It should be noted that after doping with iron and nitrogen (ACP) I_D/I_G was increased to a value of 1.24, implying a considerable increase in defect density. I_D/I_G was marginally reduced after ball milling and acid washing (ACPE) to ~ 1.21 . Higher defect density in ACP outlines a possibility of enhanced ORR due to the defect/edge engineering approach.

In order to examine the chemistry of prepared electrocatalysts from scrap tires, FTIR spectroscopy was employed and the obtained spectra are demonstrated in Figure 3b. FTIR trends of all the samples are quite similar in shapes with nearly consistent peak positions, however, the intensity of some peaks increases with subsequent steps in the sample fabrication design. It is worth mentioning that usually oscillation frequencies of ideal sp^2 graphitic domains are weaker in the infrared range as they don’t change their dipole moments. Whereas the presence of defects in the form of superficial edges, heteroatomic substitutions, radical species, or surface functionalities give rise to IR-active modes [59]. Generally, the region of higher wavenumber in the range of $3800\text{--}3000$ cm^{-1} is linked with the occurrence of hydroxyl functionalities [60]. Interestingly, no

appreciable bands were obtained in this range, except in the case of ACP and ACPE, where a minor band in the vicinity of 3451 cm^{-1} was evolved which could be attributed to O-H vibrations of hydroxyl species or adsorbed water [61]. Next, the three peaks in the proximity of 3016 cm^{-1} , 2970 cm^{-1} , and 2935 cm^{-1} indicates the presence of C-H bonds [62]. Peaks approximately at 2355 cm^{-1} and 2326 cm^{-1} (marked with *) emerged due to adsorption of carbon dioxide into the sample from the surrounding environment [1,7]. Moreover, in ACP and ACPE a tiny peak $\sim 2147\text{ cm}^{-1}$ can be related to C=N [63]. As moving further towards the lower wavenumber, a very strong peak at 1735 cm^{-1} gives an impression of C=O stretching from carboxyl and/or carbonyl functionalities [64,65]. Band located at $\sim 1435\text{ cm}^{-1}$ can be designated to cm^{-1} to bending of C-H groups [25]. Around 1365 cm^{-1} , another strong peak can be appreciated from the FTIR spectra, getting more intense in ACP and ACPE. This peak can be assigned either to C-N [66] or CH_3 of methyl species [67]. This supposition can be supported by the fact that nitrogen was intentionally doped in ACP and ACPE to develop Fe- N_x moieties and also the corresponding 'D' peaks in Raman spectra of these two samples were comparatively increased indicating the enhancement of carbon defects. The presence of N in ACP and ACPE was also confirmed by TEM elemental area mapping and CHNS analysis (Table S2). Finally, an FTIR peak located at $\sim 1213\text{ cm}^{-1}$ appears due to C-O stretching [61] this peak can also appear due to asymmetrical stretching of C-N together with NH_2 (out of plan) [68]. The peak corresponding to $\sim 1213\text{ cm}^{-1}$ was intensified in the case of ACP and ACPE which were doped with N.

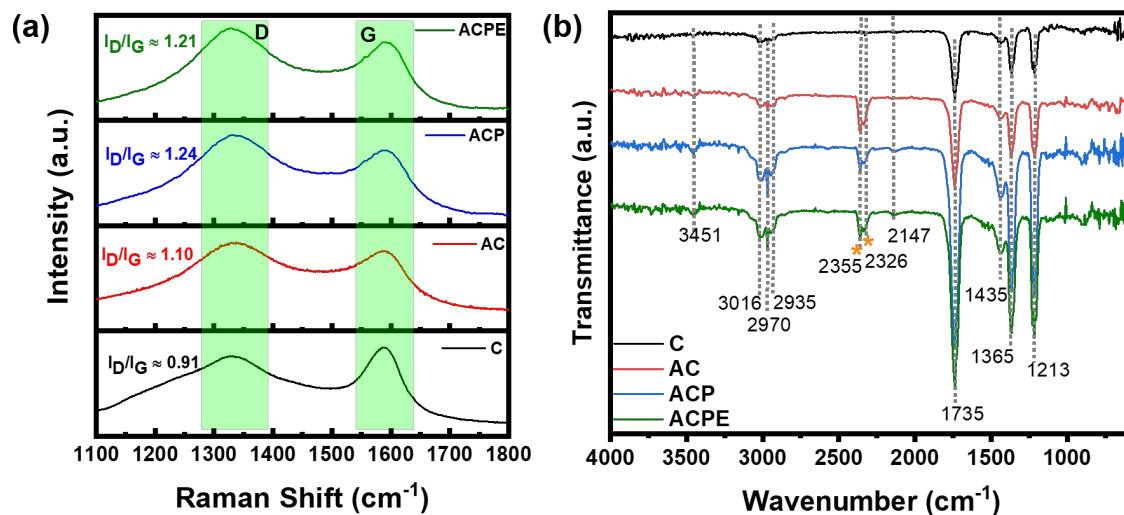


Figure 3. Raman spectra (a) and FTIR spectra (b) of developed samples, peaks marked with asterisks correspond to ambient CO₂.

To further explore the surface chemistry of the derived electrocatalysts, XPS was employed. Table 2 summarizes the atomic composition of the four samples, while Figure S3 in the *Supplementary Information* shows the survey spectra. As highlighted also by XRD and FITR analyses, all the four samples were mostly composed of carbon and oxygen. Sulfur and zinc were present in small amounts only in sample C and they disappeared in the next three samples, due to the activation and functionalization steps. Nitrogen could be detected only in the final ACPE sample whereas Fe remained undetected through XPS analysis.

Table 2. XPS atomic percentage concentration of the prepared samples

Atomic %	C	AC	ACP	ACPE
C 1s	94.7	91.2	96.5	88.8
N 1s	n.d.	n.d.	n.d.	2.0
O 1s	3.2	8.8	3.5	9.1
S 2p	1.1	n.d.	n.d.	0.1

Zn 2p3	0.6	n.d.	n.d.	n.d.
Cl 2p	0.4	n.d.	n.d.	n.d.

High-resolution C 1s, O 1s and N 1s spectra were deconvoluted based on previous studies [50,69,70] and Table S3 in the *Supplementary Information* lists the main elements peak binding energies and relative areas obtained. The presence of oxygen and defect-rich structure especially zigzag edges may affect the assignment of peak position in nitrogen-doped carbon-based structure therefore a careful analysis is required [71]. Figure 4 shows the high-resolution C 1s, O 1s and N 1s spectra of the final sample ACPE, while Figure S4 in the *Supplementary Information* shows the C 1s and O 1s high-resolution spectra of the samples C, AC and ACP. About carbon moieties, graphitic carbon came out to be predominant in all samples, as confirmed also by TEM and FTIR analyses. The amount of graphitic carbon was slightly decreased following the activation and functionalization of the tires which is consistent with Raman's outcomes. Graphitic carbon is beneficial for corrosion resistance. The presence of oxygenated species on samples AC, ACP and ACPE demonstrates effective doping of graphene layers with defects [72], also confirmed by analyzing the oxygen moieties. About nitrogen moieties, they were detectable only in the final sample ACPE (Figure 4c). Here, the ratio N pyridinic/N pyrrolic was relatively high, equal to 1.2, while the graphitic nitrogen was relatively low. The deconvolution of the spectrum also highlighted N-Me coordination equal to 26.6%, which was embedded in the carbon matrix. It is already established that N pyridinic and N-Me are the most active sites to carryout ORR in all three pH [35,43,73]. The Fe 2p peak was not detected which might be due to the very low concentration that could be below the detection limit of the instrument. Moreover, in ACPE detection of N-Me species in appreciable proportion gives an impression of atomically dispersed Fe coordinated nitrogen.

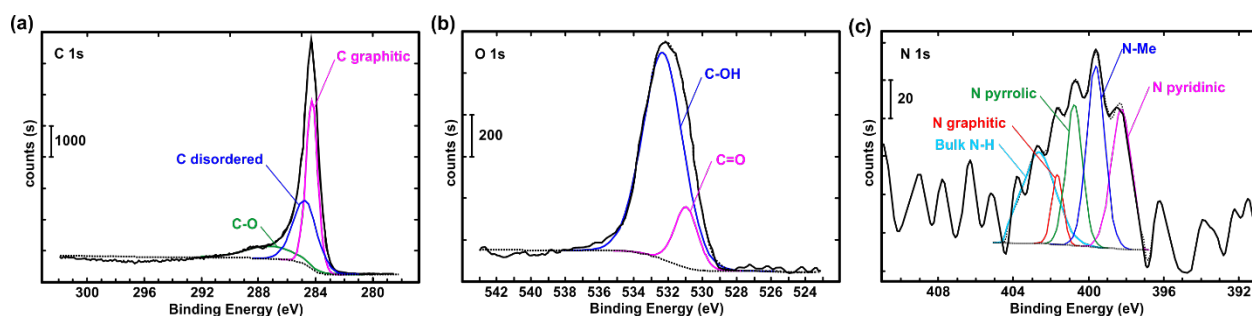
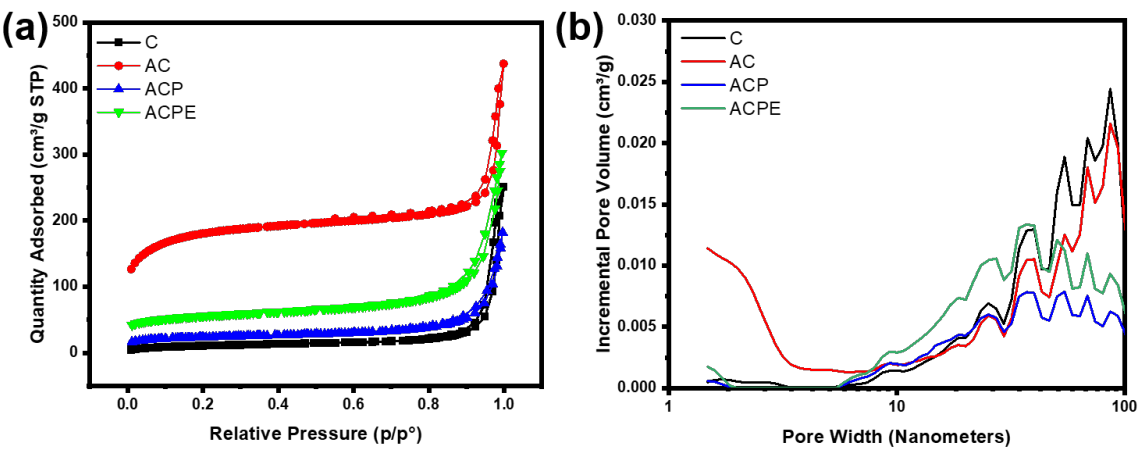


Figure 4. XPS high-resolution spectra of C 1s (a), O 1s (b) and N 1s (c) for the sample APCE.

The evaluation of the textural properties was carried out by analyzing the N_2 adsorption/desorption isotherms at 77 K that are reported in Figure 5a. At low pressures, the isotherm branches of the AC sample illustrated sharp adsorption inflections which are indicative of type I and materials containing micropores. Adsorption at the lowest relative pressure decreases in the order $ACPE > ACP > C$ suggesting a parallel decrease of the microporosity. However, at higher relative pressures ($P/P_0 > 0.2$), the carbons displayed type IV isotherm adsorption-desorption branches showing the existence of mesopores. In addition, for all the samples the sharp adsorption at $P/P_0 > 0.9$ is representative of the presence of large mesopores and macropores. These observations are confirmed by the DFT pore size distribution that is reported in terms of incremental pore volume in Figure 5b. The micropore volume (V_{micro}), mesopore volume (V_{meso}), and total pore volume (V_{total}) of the different samples are charted in Table 3 along with the BET surface area (S_{BET}). The highest V_{micro} of $0.204 \text{ cm}^3 \text{ g}^{-1}$ is achieved with AC. Given that micropores are the class of pores that mainly affect the specific surface area, AC is also the sample with the highest S_{BET} of $671 \text{ m}^2 \text{ g}^{-1}$. The massive increment in the BET surface area of pristine carbon after activation, from $26.8 \text{ m}^2 \text{ g}^{-1}$ to $671 \text{ m}^2 \text{ g}^{-1}$, highlights the effectiveness of the activation step since the engineering of the carbon matrix is an important turning point in the uplifting of ORR activity by granting easy access to the electrochemically active sites. However, after the high-temperature pyrolysis (ACP) a prominent decrease in the corresponding BET surface area ($85.3 \text{ m}^2 \text{ g}^{-1}$) was witnessed, which might be due to structural rearrangements at a higher temperature and in parallel the addition of nitrogen-containing organic molecules and, mainly, of iron oxide that might have occluded the pores and contribute to the sample mass. An additional interesting feature to recognize is the sufficient restoration of surface area with a predominance of micro-mesoporosity after ball milling and acid washing (ACPE) as shown in Figure 5b. The BET surface area of ACPE was estimated to be $204 \text{ m}^2 \text{ g}^{-1}$. Higher surface area and increase in the porosity could be a result of Fe_3O_4 nanoparticles removal due to the leaching effect of ball-milling and acid etching. As it concerns the meso-macropore range, the pore size distribution of C and AC are similar. After activation, the meso-macropore PSD does not significantly change, but the number of meso-macropores decreases in favor of the increase of the number of micropores. In ACP, V_{tot} is lower than in AC, mainly because of the decrease of the number of the largest mesopores ($>30 \text{ nm}$) and macropores. In ACPE, the removal of Fe_3O_4 nanoparticles almost doubles the specific volume not only from micropores but also from meso and macropores



477

478 **Figure 5.** N₂ adsorption-desorption isotherms (a) and pore size distribution (b) of the as-developed
479 samples

480

481 **Table 3.** DFT micropore volume (V_{micro}), mesopore volume (V_{meso}), and total pore volume (V_{total}),
482 and BET specific surface area (S_{BET}), of the different samples

Samples	$V_{\text{micro}} (<2\text{nm})$ cm^3g^{-1}	$V_{\text{meso}} (2 -50 \text{ nm})$ cm^3g^{-1}	V_{total} cm^3g^{-1}	S_{BET} $\text{m}^2 \text{g}^{-1}$
C	0.003	0.143	0.372 (<400 nm)	26.8
AC	0.204	0.168	0.611 (< 400 nm)	671
ACP	0.018	0.112	0.233 (<300 nm)	85.3
ACPE	0.047	0.190	0.359 (<200 nm)	204

483

484 **3.2. Electrochemical performance of scrap tires derived electrocatalysts**

485 To elucidate the electrocatalytic activity of derived electrocatalysts, RRDE operating at
486 1600 rpm was performed. Three different oxygen-saturated electrolytes: acidic, neutral, and
487 alkaline media were used since the mechanism of ORR differs by varying the pH of the electrolyte
488 [41,74–76] Moreover, to analyze the effect of catalyst loading on the ORR kinetics, two different
489 loadings of 0.2 mg cm^{-2} and 0.6 mg cm^{-2} were used and the achieved trends are illustrated in [Figure](#)
490 [S5](#) and [Figure 6](#), respectively. RRDE response typically originates in sigmoidal linear sweep

voltammograms (LSVs) where disk current varies with respect to the applied potential, increasing the overpotentials. Onset potential (E_{onset}), half-wave potential ($E_{1/2}$) and diffusion limiting current density (J_{lim}) are the common performance parameters defined by LSVs whereas lower peroxide yield and electron transfer number near to 4 (estimated by monitoring the ring and disk current) rationalize the utility of electrocatalysts for practical application in fuel cells [77]. In the given study, E_{onset} was measured at the current density of 0.1 mA cm^{-2} while the $E_{1/2}$ was estimated through the first derivative method.

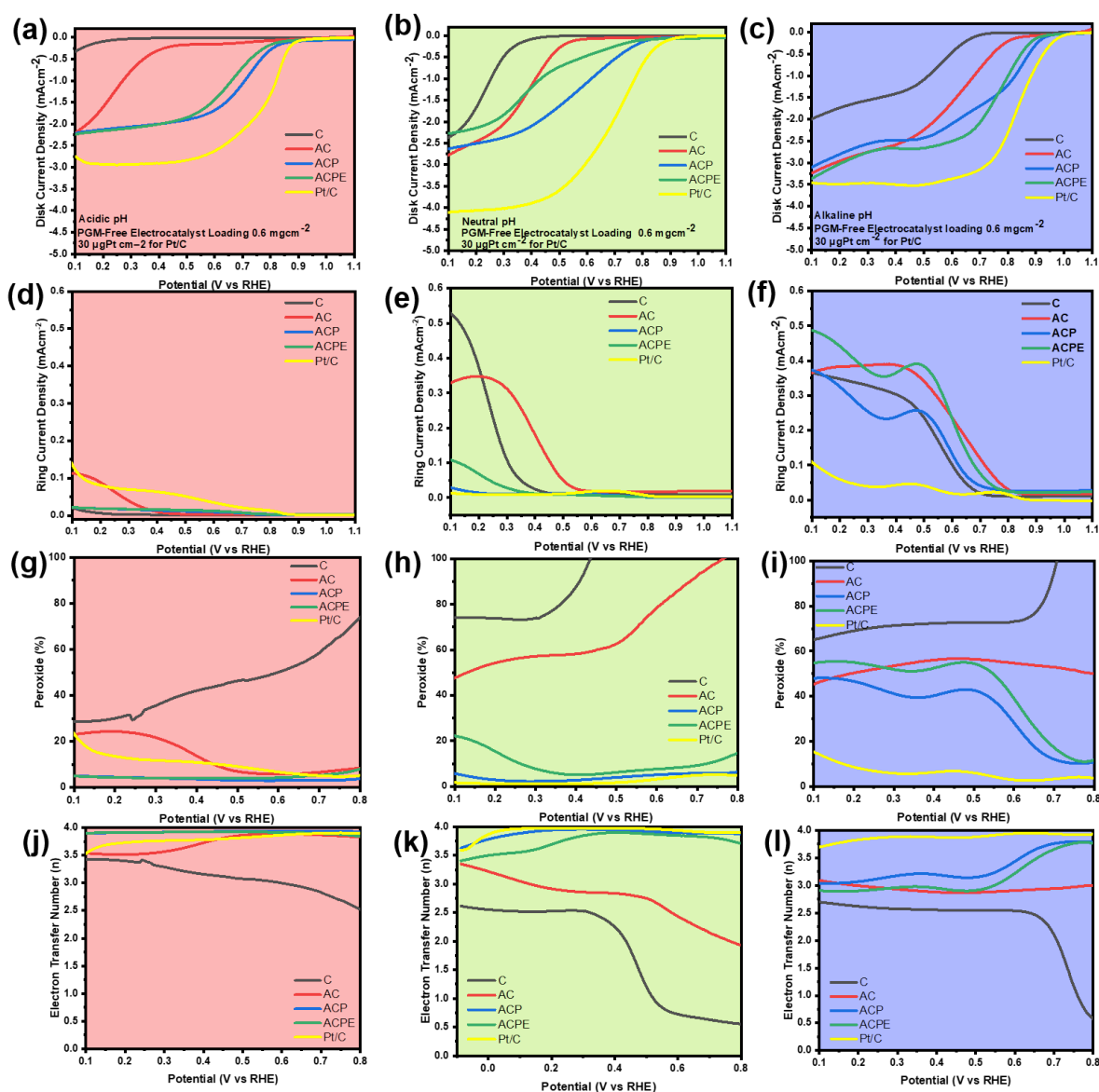


Figure 6. Electrocatalytic activity of the scrap tires derived ORR electrocatalysts in oxygen-saturated acidic (red), neutral (light green), and alkaline (blue) media. linear sweep voltammograms (a-c), ring current densities with respect to applied potential (d-f), trends of electron transfer (g-i), and peroxide production (j-l) during the electro-reduction of oxygen in the respective electrolytes with a PGM-free electrocatalyst loading of 0.6 mg cm^{-2} and $30 \text{ } \mu\text{gPt cm}^{-2}$ for the benchmark Pt/C. The scan rate was maintained at 5 mV s^{-1} while the rotation speed of RRDE was kept at 1600 rpm.

3.2.1 Electrocatalytic activity in acid media

The first panel of **Figure 6** (graphs with red backgrounds) demonstrates the ORR activity of electrocatalysts achieved at different stages of the experimental design in oxygen-saturated $0.5 \text{ M H}_2\text{SO}_4$. From LSVs presented in **Figure 6a** and **Figure S5a**, the pristine sample ‘C’ and AC showed very insubstantial activities towards ORR by offering very high overpotentials. However, iron and nitrogen doping noticeably uplifted the reaction kinetics with a well-defined diffusion limiting current plateaus. In comparison with C and AC, samples at successive synthesis stages had categorically higher E_{onset} and $E_{1/2}$, defining the effectiveness of nitrogen and iron doping. With an electrocatalyst loading of 0.2 mg cm^{-2} , ACP and ACPE demonstrated E_{onset} of about 0.801 and 0.767 V vs RHE , respectively, where the $E_{1/2}$ was estimated to be at 0.646 and 0.537 V vs RHE , respectively. When the loading was increased from 0.2 to 0.6 mg cm^{-2} , the kinetics of ORR activity was further enhanced and the E_{onset} of ACP reached up to 0.881 V vs RHE with appreciable diffusion limiting current density and $E_{1/2}$. As witnessed from TEM, the embedment of Fe-based nanoparticles in carbon matrix having a higher degree of graphitic disorders (also confirmed by Raman spectroscopy, FTIR and XPS) might be the possible reason for the favorable electro-reduction of oxygen in the case of ACP. Electrocatalyst loading also had a positive effect on the peroxide yield which was considerably diminished due to an increase in loading. For the sample ACP, peroxide production remained restricted to a maximum $\sim 5\%$ within the potential window of 0.1 to 0.8 V vs RHE whereas ACPE showed slightly higher peroxide generation at the start (with 0.6 mg cm^{-2} loading on RRDE). In general, an increase in electrocatalyst loading led to a decrease in peroxide production. This phenomenon has been previously shown [78–80] and it infers that the produced peroxide is consumed within the thicker electrocatalytic layer without escaping. The trends of electron transfer presented in **Figure S5j** and **Figure 6j** further endorse the

occurrence of the tetra-electronic ORR pathway followed by Fe-N-Cs in acidic media. The electron transfer number for ACP came out to be ~ 3.74 - 3.8 and ~ 3.9 - 3.93 with the loading of 0.2 and 0.6 mg cm^{-2} , respectively. ACPE showed a slightly lower number of electrons transferred nearly 3.4 - 3.78 and 3.84 - 3.89 with the loading of 0.2 and 0.6 mg cm^{-2} , respectively. Although the kinetic performance of the derived PGM-free electrocatalysts remained inferior compared to that of benchmark Pt/C ($20 \text{ wt.}\%$), interestingly ACP and ACPE outperformed Pt/C by yielding lower peroxide together with superior trends in electron transfer. This observation can be attributed to the presence of active sites favoring the tetra-electronic ORR at lower pH.

3.2.2 Electrocatalytic activity in neutral media

RRDE measurements in neutral conditions provide insights for the employment of electrocatalysts for ORR in microbial FCs (MFCs) in which polluted water can be used for power generation using bioelectrochemical systems. Deactivation of PGM in polluted and anions-carrying neutral electrolytes launch a technological interest in non-PGM electrocatalysts for MFCs [81,82]. Therefore, ORR activity of developed electrocatalysts was also analyzed in the neutral media (0.1 M PBS) and the achieved trends with 0.2 and 0.6 mg cm^{-2} electrocatalyst loading are presented in the central panel (graphs with light green background) of Figure S5 and Figure 6, respectively. Although the trends of oxygen reduction were similar to those obtained for the acidic media, the E_{onset} and $E_{1/2}$ were a bit delayed, depicting relatively slower ORR kinetics. In fact, the neutral electrolytic solution has a considerably lower concentration of ionic species (i.e. H^+ and OH^-) which usually impede ORR performance by offering higher overpotentials [78]. From LSVs given in Figure S5b and Figure 6b, again ACP outperformed the other PGM-free counterparts with E_{onset} of 0.792 V vs RHE and 0.822 V vs RHE with electrocatalyst loading of 0.2 and 0.6 mg cm^{-2} , respectively. Moreover, ACP produced ~ 2.3 - 6.3% peroxide (Figure 6h) which slightly increased as the loading was decreased to 0.2 mg cm^{-2} where the electron transfer number was always above 3.8 . It is pertinent to note that ACP showed a nearly similar tendency of peroxide generation and electron transformation during ORR at neutral pH nearly as demonstrated by Pt/C. Overall activity in the neutral media followed a descending order of $\text{Pt/C} > \text{ACP} > \text{ACPE} > \text{AC} > \text{C}$. Once again, the increase in the electrocatalyst loading led to better electrocatalytic activity, lower peroxide production and a higher number of electrons exchanged, in agreement with previous literature [73,80,83,84].

3.2.3 Electrocatalytic activity in alkaline media

The ORR electrocatalytic activities of derived electrocatalysts were additionally monitored in 0.1 M KOH since alkaline conditions favor the performance of TM-N-C electrocatalysts diminishing the existing gaps with PGM electrocatalysts [77]. Hence, an advanced class of FCs i.e. anion-exchange membrane FC (AEMFCs) has emerged where scarce and expensive Pt-based electrocatalysts can be successfully replaced with PGM-free. ORR behavior of the fabricated electrocatalysts in alkaline media is presented in the third panel (with blue background) of Figure 6 and Figure S5. It is worth mentioning that the overall trend of LSVs in alkaline media is similar to that obtained in the other two media, but all the curves are shifted towards lower overpotentials, representing relatively higher E_{onset} and $E_{1/2}$. As expected again the benchmark Pt/C having the highest E_{onset} and J_{lim} kinetically beat the PGM-free electrocatalysts like in acidic and neutral media however, skyrocketing price and scarcity of the PGMs cannot justify their employment in fuel cells. On the other hand, the order of ORR activity in 0.1 M KOH evolved as ACP>ACPE>AC>C corresponding to 0.6 mg cm⁻² loading of the PGM-Free electrocatalysts. ACP showed a remarkable E_{onset} of 0.917 V vs RHE together with $E_{1/2}$ of 0.841 V vs RHE at the loading of 0.2 mg cm⁻² on RRDE. As the electrocatalyst loading increased, the E_{onset} and $E_{1/2}$ of ACP were further improved to 0.936 and 0.852 V vs RHE, respectively. Higher $E_{1/2}$ during ORR measurements in 0.1 M KOH might be due to the partial contribution of HO₂[•] having higher stability on the Fe⁺² carrying active sites compared to H₂O₂ (peroxide intermediation produces in acidic conditions) [85]. From the ring, current densities for all the electrocatalysts sharply increase with a decrease in potential values and an obvious effect of this phenomenon on peroxide yield can be appreciated in Figure 6i and Figure S5i. It is important to underline that, as compared to 0.5 M H₂SO₄ peroxide production was significantly increased by 0.1 M KOH for all the developed electrocatalysts. Similar results have recently been reported by Daniel et al. for waste-polyurethane-derived Fe-N-Cs [24]. They also experienced a preferential tetra-electronic reduction of O₂ to H₂O with a peroxide yield of less than 5% in acidic media whereas peroxide selectivity was raised up to 60% in an alkaline environment. A few years back, Rojas-Carbonell and coworkers endeavored to establish a correlation among ORR activity, surface chemistry and pH of the electrolyte [41]. They found that it is the concentration of protons and hydroxyls present in the electrolyte which could alter the surface chemistry of the electrocatalysts and hence overall reaction mechanism changed

importantly due to which selectivity of the electrocatalyst varies with the pH changes [41]. Zhong et al. combined the theoretical and experimental investigations to analyze the physicochemical interaction of H^+ and OH^- ions with the surface of electrocatalysts [75]. According to their DFT calculations, the adsorption of H^+ ions on Fe-sites are thermodynamically unfavorable conversely, OH^- as a strong Lewis base makes a robust bonding with iron due to the negative free energy of adsorption. The retarding effect due to adsorption of OH^- is more pronounced on the Edge- FeN_4 moieties because of their higher coordination ability owing to flexible structure [75]. Furthermore, N. Ramaswamy and S. Mukerjee explained the shifting of the ORR mechanism from inner-sphere to outer-sphere electron transfer which predominately leads to the formation of a large amount of peroxide intermediate as the ultimate product [74]. In any case, it is important to highlight the electron transfer number remained again highest for ACP in 0.1 M KOH as well and with higher loading, it was always above 3.

From the analyzed electrocatalytic performance and structural parameters of the developed electrocatalysts, it is confirmed that doping of iron and nitrogen has a marked influence on the ORR activity, implying the tetra-electron pathway of ORR in acidic and neutral conditions. Although the $E_{1/2}$ and E_{onset} potential in alkaline conditions are superior, greater peroxide yield is still challenging. The best performance of ACP is ascribed to Fe_3O_4 nanoparticles embedded in the graphitic matrix having a lot of structural defects, representing robust active sites for ORR. However, the final step in the catalyst fabrication involving ball milling and acid washing after the high-temperature pyrolysis (ACPE) negatively affects the performance. The most probable speculation could be a sufficient removal of Fe_3O_4 nanoparticles along with a little restoration of graphitization in ACPE as verified through XRD and Raman spectroscopy, respectively. The leaching of iron-based nanoparticles from the carbon framework could reduce the ORR activity [86]. Such kind of activation loss during the acid washing of Fe-N-Cs has been thoroughly analyzed by Singh and coworkers who experienced continuous leaching of Fe leaching as long as the electrocatalyst was immersed in the acidic solution [87]. Moreover, Xu et al. also reported the higher electrocatalytic activity of iron oxide embedded Fe-N-Cs in acidic and alkaline media mainly due to encapsulation of iron oxide particles in graphitic carbon which was significantly reduced after ball-milling and acid washing [56]. Apparently, such tightly wrapped iron-based nanoparticles are not in direct contact with the surrounding electrolyte, however, they can effectively activate the surrounding carbon and are very helpful in uplifting the ORR kinetics

[56,88]. Likewise, encapsulation of metal oxide nanoparticles in carbon layers could also provide structural robustness and superior electrochemical stability by preventing the corrosive dissolution and redeposition of metallic nanoparticles during oxygen reduction [23,56]. Such structural attributes were confirmed in the ACP through detailed characterizations and might be the possible reasons for enhanced activity compared to ACPE whose ORR performance was slightly reduced during acid washing.

In addition to favorable electrocatalytic activity, operational durability is another aspect to be assessed while developing a promising electrocatalyst. Therefore, short-term stability tests of the best performing electrocatalyst i.e. ACP over 2500 cycles were executed in all three media using a similar RRDE methodology. Achieved trends are displayed in Figure S6, where ACP exhibited continuous kinetic degradation in every electrolyte since $E_{1/2}$ was shifting negatively with incremental cycling. After the first 500 cycles, a prominent decrease in the $E_{1/2}$ was experienced. This might be attributed to the leaching of the Fe from exposed nanoparticles [89,90]. After 2500 cycles the final decay in $E_{1/2}$ at the end often in acidic, neutral and alkaline conditions came out to be ~86, ~240 and ~21 mV, respectively. Quite interestingly changes in the peroxide yield and electron transference were not significant which still confirms the performance selectivity of ACP despite the lowering of $E_{1/2}$ over the period. The increase in peroxide yield at the end of the stability test in the vicinity of J_{lim} at ~0.2 V was estimated at ~5.7%, ~0.43% and 14.3% for acidic, neutral and alkaline electrolytes. Hitherto Fe-N-C owing to their incredible activity and cost-effectiveness demonstrate great potential for the replacement of PGMs, however, their limited stability and multiple degradation mechanisms of complex nature require further insights [89–92]. No doubt studying the exact mechanism involved in electrocatalytic decay and the robustness factor of the active moieties in the waste-derived Fe-N-Cs is an important task, however, it lies outside the scope of the current study and might be followed separately.

Conclusions

In a summary, char derived from scrap tires through the MAP technique was used as a cost-effective precursor for the synthesis of Fe-N-C. Chemical activation of char using KOH ensured a sufficient increase in surface area and formation of the micro-macroporous environment as confirmed by BET analysis. High-temperature pyrolysis successfully functionalized the activated carbon with iron and nitrogen where the fabricated ACP was composed of highly efficient Fe_3O_4

nanoparticles embedded in a carbon matrix having a high graphitic disorder, hence exhibiting the best ORR performance. To demonstrate the efficacy of developed electrocatalysts towards FCs application, ORR activity was elucidated in three different electrolytic conditions; acidic, neutral, and alkaline, using two electrocatalyst loadings of 0.2 and 0.6 mg cm⁻². An increase in electrocatalyst loading further uplifted ORR kinetics and turned down the peroxide yield. ORR activity was substantially reduced after ball-milling and acid washing mainly due to the removal of iron oxide particles from the Fe-N-C structural framework. ACP manifests outstanding E_{onset} of 0.881, 0.822 and 0.936 V vs RHE in acidic, neutral, and alkaline conditions with 0.6 mg cm⁻² loading on RRDE. Peroxide yield was lower in acidic (~ 5%) and neutral (~ 6.3%) media, implying the tetra-electronic pathway with an electron transfer number close to 4. However, in the alkaline medium, the peroxide yield was considerably increased probably due to the shifting of the ORR mechanism. Although ACP demonstrated high electrocatalytic activity in all three media, its operational durability still remained challenging and requires further insights.

Declaration of Competing Interest

The authors declare that they have no known competing financial interests or personal relationships that could have appeared to influence the work reported in this paper.

Acknowledgment

Carlo Santoro would like to thank the support from the Italian Ministry of Education, Universities and Research (Ministero dell'Istruzione, dell'Università e della Ricerca – MIUR) through the “Rita Levi Montalcini 2018” fellowship (Grant number PGR18MAZLI). Financial support from the Italian Ministry of University and Research (MIUR) through grant “Dipartimenti di Eccellenza – 2017 – Materials for energy” is gratefully acknowledged. The authors also thank the Italian ministry MIUR for funding through the FISR 2019 project AMPERE (FISR2019_01294).

References

- [1] R. Gómez-Hernández, Y. Panecatl-Bernal, M.Á. Méndez-Rojas, High yield and simple one-step production of carbon black nanoparticles from waste tires, *Heliyon*. 5 (2019) e02139. <https://doi.org/10.1016/j.heliyon.2019.e02139>.

- [2] B.S. Thomas, R.C. Gupta, V.J. Panicker, Recycling of waste tire rubber as aggregate in concrete: durability-related performance, *Journal of Cleaner Production*. 112 (2016) 504–513. <https://doi.org/10.1016/j.jclepro.2015.08.046>.
- [3] B.S. Thomas, R.C. Gupta, P. Mehra, S. Kumar, Performance of high strength rubberized concrete in aggressive environment, *Construction and Building Materials*. 83 (2015) 320–326. <https://doi.org/10.1016/j.conbuildmat.2015.03.012>.
- [4] A. Sofi, Effect of waste tyre rubber on mechanical and durability properties of concrete – A review, *Ain Shams Engineering Journal*. 9 (2018) 2691–2700. <https://doi.org/10.1016/j.asej.2017.08.007>.
- [5] C.-C. Chen, T. Yamada, I.-M. Chiu, Y.-K. Liu, Evaluation of the Waste Tire Resources Recovery Program and Environmental Health Policy in Taiwan, *Int J Environ Res Public Health*. 6 (2009) 1075–1094. <https://doi.org/10.3390/ijerph6031075>.
- [6] J. Kirchherr, D. Reike, M. Hekkert, Conceptualizing the circular economy: An analysis of 114 definitions, *Resources, Conservation and Recycling*. 127 (2017) 221–232. <https://doi.org/10.1016/j.resconrec.2017.09.005>.
- [7] R.B. González-González, L.T. González, S. Iglesias-González, E. González-González, S.O. Martinez-Chapa, M. Madou, M.M. Alvarez, A. Mendoza, Characterization of Chemically Activated Pyrolytic Carbon Black Derived from Waste Tires as a Candidate for Nanomaterial Precursor, *Nanomaterials*. 10 (2020) 2213. <https://doi.org/10.3390/nano10112213>.
- [8] A. Evans, R. Evans, The Composition of a Tyre: Typical Components, The Old Academy, 21 Horse Fair, Banbury, Oxon OX16 0AH, 2006.
- [9] B.-C. Yu, J.-W. Jung, K. Park, J.B. Goodenough, A new approach for recycling waste rubber products in Li–S batteries, *Energy Environ. Sci*. 10 (2017) 86–90. <https://doi.org/10.1039/C6EE02770A>.
- [10] A.K. Naskar, Z. Bi, Y. Li, S.K. Akato, D. Saha, M. Chi, C.A. Bridges, M.P. Paranthaman, Tailored recovery of carbons from waste tires for enhanced performance as anodes in lithium-ion batteries, *RSC Adv*. 4 (2014) 38213–38221. <https://doi.org/10.1039/C4RA03888F>.
- [11] Z.D. Hood, X. Yang, Y. Li, A.K. Naskar, M. Chi, M.P. Paranthaman, Conversion of Waste Tire Rubber into High-Value-Added Carbon Supports for Electrocatalysis, *J. Electrochem. Soc*. 165 (2018) H881. <https://doi.org/10.1149/2.1081813jes>.

- [12] M. Zhi, F. Yang, F. Meng, M. Li, A. Manivannan, N. Wu, Effects of Pore Structure on Performance of An Activated-Carbon Supercapacitor Electrode Recycled from Scrap Waste Tires, *ACS Sustainable Chem. Eng.* 2 (2014) 1592–1598. <https://doi.org/10.1021/sc500336h>.
- [13] H.A. Firouzjaie, W.E. Mustain, Catalytic Advantages, Challenges, and Priorities in Alkaline Membrane Fuel Cells, *ACS Catal.* 10 (2020) 225–234. <https://doi.org/10.1021/acscatal.9b03892>.
- [14] Z. Jiang, J. Yu, T. Huang, M. Sun, Recent Advance on Polyaniline or Polypyrrole-Derived Electrocatalysts for Oxygen Reduction Reaction, *Polymers.* 10 (2018) 1397. <https://doi.org/10.3390/polym10121397>.
- [15] C. Ouyang, X. Wang, Recent progress in pyrolyzed carbon materials as electrocatalysts for the oxygen reduction reaction, *Inorganic Chemistry Frontiers.* 7 (2020) 28–36. <https://doi.org/10.1039/C9QI00962K>.
- [16] S.T. Thompson, B.D. James, J.M. Huya-Kouadio, C. Houchins, D.A. DeSantis, R. Ahluwalia, A.R. Wilson, G. Kleen, D. Papageorgopoulos, Direct hydrogen fuel cell electric vehicle cost analysis: System and high-volume manufacturing description, validation, and outlook, *Journal of Power Sources.* 399 (2018) 304–313. <https://doi.org/10.1016/j.jpowsour.2018.07.100>.
- [17] M.-X. Chen, L. Tong, H.-W. Liang, Understanding the Catalytic Sites of Metal–Nitrogen–Carbon Oxygen Reduction Electrocatalysts, *Chem. Eur. J.* 27 (2021) 145–157. <https://doi.org/10.1002/chem.202002427>.
- [18] W. Wang, Q. Jia, S. Mukerjee, S. Chen, Recent Insights into the Oxygen-Reduction Electrocatalysis of Fe/N/C Materials, *ACS Catal.* 9 (2019) 10126–10141. <https://doi.org/10.1021/acscatal.9b02583>.
- [19] S. Li, S.-H. Ho, T. Hua, Q. Zhou, F. Li, J. Tang, Sustainable biochar as an electrocatalysts for the oxygen reduction reaction in microbial fuel cells, *Green Energy & Environment.* (2020). <https://doi.org/10.1016/j.gee.2020.11.010>.
- [20] M. Jiang, X. Yu, H. Yang, S. Chen, Optimization Strategies of Preparation of Biomass-Derived Carbon Electrocatalyst for Boosting Oxygen Reduction Reaction: A Minireview, *Catalysts.* 10 (2020) 1472. <https://doi.org/10.3390/catal10121472>.

- [21] M. Muhyuddin, P. Mustarelli, C. Santoro, Recent Advances in Waste Plastic Transformation into Valuable Platinum-Group Metal-Free Electrocatalysts for Oxygen Reduction Reaction, *ChemSusChem*. 14 (2021) 3785–3800. <https://doi.org/10.1002/cssc.202101252>.
- [22] J. Munuera, L. Britnell, C. Santoro, R. Cuéllar-Franca, C. Casiraghi, A review on sustainable production of graphene and related life cycle assessment, *2D Mater.* 9 (2021) 012002. <https://doi.org/10.1088/2053-1583/ac3f23>.
- [23] N. Cai, S. Xia, X. Zhang, Z. Meng, P. Bartocci, F. Fantozzi, Y. Chen, H. Chen, P.T. Williams, H. Yang, Preparation of Iron- and Nitrogen-Codoped Carbon Nanotubes from Waste Plastics Pyrolysis for the Oxygen Reduction Reaction, *ChemSusChem*. 13 (2020) 938–944. <https://doi.org/10.1002/cssc.201903293>.
- [24] G. Daniel, T. Kosmala, M.C. Dalconi, L. Nodari, D. Badocco, P. Pastore, A. Lorenzetti, G. Granozzi, C. Durante, Upcycling of polyurethane into iron-nitrogen-carbon electrocatalysts active for oxygen reduction reaction, *Electrochimica Acta*. 362 (2020) 137200. <https://doi.org/10.1016/j.electacta.2020.137200>.
- [25] J.C. Park, J.-C. Kim, S. Park, D.-W. Kim, Efficient waste polyvinyl(butylal) and cellulose composite enabled carbon nanofibers for oxygen reduction reaction and water remediation, *Applied Surface Science*. 510 (2020) 145505. <https://doi.org/10.1016/j.apsusc.2020.145505>.
- [26] J.G.S. Moo, A. Veksha, W.-D. Oh, A. Giannis, W.D.C. Udayanga, S.-X. Lin, L. Ge, G. Lisak, Plastic derived carbon nanotubes for electrocatalytic oxygen reduction reaction: Effects of plastic feedstock and synthesis temperature, *Electrochemistry Communications*. 101 (2019) 11–18. <https://doi.org/10.1016/j.elecom.2019.02.014>.
- [27] A. Veksha, K. Yin, J.G.S. Moo, W.-D. Oh, A. Ahamed, W.Q. Chen, P. Weerachanchai, A. Giannis, G. Lisak, Processing of flexible plastic packaging waste into pyrolysis oil and multi-walled carbon nanotubes for electrocatalytic oxygen reduction, *Journal of Hazardous Materials*. 387 (2020) 121256. <https://doi.org/10.1016/j.jhazmat.2019.121256>.
- [28] M. Muhyuddin, J. Filippi, L. Zoia, S. Bonizzoni, R. Lorenzi, E. Berretti, L. Capozzoli, M. Bellini, C. Ferrara, A. Lavacchi, C. Santoro, Waste Face Surgical Mask Transformation into Crude Oil and Nanostructured Electrocatalysts for Fuel Cells and Electrolyzers, *ChemSusChem*. 15 (2022) e202102351. <https://doi.org/10.1002/cssc.202102351>.
- [29] M. Passaponti, L. Rosi, M. Savastano, W. Giurlani, H.A. Miller, A. Lavacchi, J. Filippi, G. Zangari, F. Vizza, M. Innocenti, Recycling of waste automobile tires: Transforming char in

oxygen reduction reaction catalysts for alkaline fuel cells, *Journal of Power Sources*. 427 (2019) 85–90. <https://doi.org/10.1016/j.jpowsour.2019.04.067>.

[30] M. Passaponti, L. Lari, M. Bonechi, F. Bruni, W. Giurlani, G. Sciortino, L. Rosi, L. Fabbri, M. Vizza, V.K. Lazarov, C. Fontanesi, M. Innocenti, Optimisation Study of Co Deposition on Chars from MAP of Waste Tyres as Green Electrodes in ORR for Alkaline Fuel Cells, *Energies*. 13 (2020) 5646. <https://doi.org/10.3390/en13215646>.

[31] A. Veksha, N.M. Latiff, W. Chen, J.E. Ng, G. Lisak, Heteroatom doped carbon nanosheets from waste tires as electrode materials for electrocatalytic oxygen reduction reaction: Effect of synthesis techniques on properties and activity, *Carbon*. 167 (2020) 104–113. <https://doi.org/10.1016/j.carbon.2020.05.075>.

[32] G.-S. Kang, G. Lee, S.Y. Cho, H.-I. Joh, D.C. Lee, S. Lee, Recycling of waste tires by synthesizing N-doped carbon-based catalysts for oxygen reduction reaction, *Applied Surface Science*. 548 (2021) 149027. <https://doi.org/10.1016/j.apsusc.2021.149027>.

[33] T. Asset, P. Atanassov, Iron-Nitrogen-Carbon Catalysts for Proton Exchange Membrane Fuel Cells, *Joule*. 4 (2020) 33–44. <https://doi.org/10.1016/j.joule.2019.12.002>.

[34] U. Tylus, Q. Jia, K. Strickland, N. Ramaswamy, A. Serov, P. Atanassov, S. Mukerjee, Elucidating Oxygen Reduction Active Sites in Pyrolyzed Metal–Nitrogen Coordinated Non-Precious-Metal Electrocatalyst Systems, *J. Phys. Chem. C*. 118 (2014) 8999–9008. <https://doi.org/10.1021/jp500781v>.

[35] K. Artyushkova, A. Serov, S. Rojas-Carbonell, P. Atanassov, Chemistry of Multitudinous Active Sites for Oxygen Reduction Reaction in Transition Metal–Nitrogen–Carbon Electrocatalysts, *J. Phys. Chem. C*. 119 (2015) 25917–25928. <https://doi.org/10.1021/acs.jpcc.5b07653>.

[36] U.I. Kramm, J. Herranz, N. Larouche, T.M. Arruda, M. Lefèvre, F. Jaouen, P. Bogdanoff, S. Fiechter, I. Abs-Wurmbach, S. Mukerjee, J.-P. Dodelet, Structure of the catalytic sites in Fe/N/C-catalysts for O₂-reduction in PEM fuel cells, *Phys. Chem. Chem. Phys.* 14 (2012) 11673–11688. <https://doi.org/10.1039/C2CP41957B>.

[37] M. Mazzucato, C. Durante, How determinant is the iron precursor ligand in Fe-N-C single-site formation and activity for oxygen reduction reaction?, *Electrochimica Acta*. 394 (2021) 139105. <https://doi.org/10.1016/j.electacta.2021.139105>.

- [38] K. Artyushkova, S. Rojas-Carbonell, C. Santoro, E. Weiler, A. Serov, R. Awais, R. Gokhale, P. Atanassov, Correlations between Synthesis and Performance of Fe-Based PGM-Free Catalysts in Acidic and Alkaline Media: Evolution of Surface Chemistry and Morphology, *ACS Applied Energy Materials*. 2 (2019). <https://doi.org/10.1021/acsaem.9b00331>.
- [39] S. Ratso, M.T. Sougrati, M. Käärrik, M. Merisalu, M. Rähn, V. Kisand, A. Kikas, P. Paiste, J. Leis, V. Sammelselg, F. Jaouen, K. Tammeveski, Effect of Ball-Milling on the Oxygen Reduction Reaction Activity of Iron and Nitrogen Co-doped Carbide-Derived Carbon Catalysts in Acid Media, *ACS Appl. Energy Mater.* 2 (2019) 7952–7962. <https://doi.org/10.1021/acsaem.9b01430>.
- [40] A. Tyagi, S. Banerjee, S. Singh, K.K. Kar, Biowaste derived activated carbon electrocatalyst for oxygen reduction reaction: Effect of chemical activation, *International Journal of Hydrogen Energy*. 45 (2020) 16930–16943. <https://doi.org/10.1016/j.ijhydene.2019.06.195>.
- [41] S. Rojas-Carbonell, K. Artyushkova, A. Serov, C. Santoro, I. Matanovic, P. Atanassov, Effect of pH on the Activity of Platinum Group Metal-Free Catalysts in Oxygen Reduction Reaction, *ACS Catal.* 8 (2018) 3041–3053. <https://doi.org/10.1021/acscatal.7b03991>.
- [42] A. Undri, S. Meini, L. Rosi, M. Frediani, P. Frediani, Microwave pyrolysis of polymeric materials: Waste tires treatment and characterization of the value-added products, *Journal of Analytical and Applied Pyrolysis*. 103 (2013) 149–158. <https://doi.org/10.1016/j.jaap.2012.11.011>.
- [43] B. Mecheri, R. Gokhale, C. Santoro, M.A. Costa de Oliveira, A. D’Epifanio, S. Licoccia, A. Serov, K. Artyushkova, P. Atanassov, Oxygen Reduction Reaction Electrocatalysts Derived from Iron Salt and Benzimidazole and Aminobenzimidazole Precursors and Their Application in Microbial Fuel Cell Cathodes, *ACS Appl. Energy Mater.* 1 (2018) 5755–5765. <https://doi.org/10.1021/acsaem.8b01360>.
- [44] B. Erable, M. Oliot, R. Lacroix, A. Bergel, A. Serov, M. Kodali, C. Santoro, P. Atanassov, Iron-Nicarbazin derived platinum group metal-free electrocatalyst in scalable-size air-breathing cathodes for microbial fuel cells, *Electrochimica Acta*. 277 (2018) 127–135. <https://doi.org/10.1016/j.electacta.2018.04.190>.
- [45] M.J. Salar Garcia, C. Santoro, M. Kodali, A. Serov, K. Artyushkova, P. Atanassov, I. Ieropoulos, Iron-streptomycin derived catalyst for efficient oxygen reduction reaction in

- ceramic microbial fuel cells operating with urine, *Journal of Power Sources*. 425 (2019) 50–59. <https://doi.org/10.1016/j.jpowsour.2019.03.052>.
- [46] H. Adabi, A. Shakouri, N. Ul Hassan, J.R. Varcoe, B. Zulevi, A. Serov, J.R. Regalbuto, W.E. Mustain, High-performing commercial Fe–N–C cathode electrocatalyst for anion-exchange membrane fuel cells, *Nat Energy*. 6 (2021) 834–843. <https://doi.org/10.1038/s41560-021-00878-7>.
- [47] J. Lilloja, M. Mooste, E. Kibena-Põldsepp, A. Sarapuu, B. Zulevi, A. Kikas, H.-M. Piirsoo, A. Tamm, V. Kisand, S. Holdcroft, A. Serov, K. Tammeveski, Mesoporous iron-nitrogen co-doped carbon material as cathode catalyst for the anion exchange membrane fuel cell, *Journal of Power Sources Advances*. 8 (2021) 100052. <https://doi.org/10.1016/j.powera.2021.100052>.
- [48] A. Serov, A.D. Shum, X. Xiao, V. De Andrade, K. Artyushkova, I.V. Zenyuk, P. Atanasov, Nano-structured platinum group metal-free catalysts and their integration in fuel cell electrode architectures, *Applied Catalysis B: Environmental*. 237 (2018) 1139–1147. <https://doi.org/10.1016/j.apcatb.2017.08.067>.
- [49] Y. Lv, F. Zhang, Y. Dou, Y. Zhai, J. Wang, H. Liu, Y. Xia, B. Tu, D. Zhao, A comprehensive study on KOH activation of ordered mesoporous carbons and their supercapacitor application, *J. Mater. Chem*. 22 (2011) 93–99. <https://doi.org/10.1039/C1JM12742J>.
- [50] S. Zago, M. Bartoli, M. Muhyuddin, G.M. Vanacore, P. Jagdale, A. Tagliaferro, C. Santoro, S. Specchia, Engineered biochar derived from pyrolyzed waste tea as a carbon support for Fe-N-C electrocatalysts for the oxygen reduction reaction, *Electrochimica Acta*. 412 (2022) 140128. <https://doi.org/10.1016/j.electacta.2022.140128>.
- [51] Y. Garsany, O.A. Baturina, K.E. Swider-Lyons, S.S. Kocha, Experimental Methods for Quantifying the Activity of Platinum Electrocatalysts for the Oxygen Reduction Reaction, *Anal. Chem*. 82 (2010) 6321–6328. <https://doi.org/10.1021/ac100306c>.
- [52] Potassium Phosphate (pH 5.8 to 8.0) Preparation and Recipe | AAT Bioquest, (n.d.). <https://www.aatbio.com/resources/buffer-preparations-and-recipes/potassium-phosphate-ph-5-8-to-8-0> (accessed January 4, 2022).
- [53] X. Yan, Y. Yao, Y. Chen, Highly Active and Stable Fe-N-C Oxygen Reduction Electrocatalysts Derived from Electrospinning and In Situ Pyrolysis, *Nanoscale Research Letters*. 13 (2018) 218. <https://doi.org/10.1186/s11671-018-2635-x>.

- [54] Y.P. Yew, K. Shameli, M. Miyake, N. Kuwano, N.B. Bt Ahmad Khairudin, S.E. Bt Mohamad, K.X. Lee, Green Synthesis of Magnetite (Fe₃O₄) Nanoparticles Using Seaweed (*Kappaphycus alvarezii*) Extract, *Nanoscale Res Lett.* 11 (2016) 276. <https://doi.org/10.1186/s11671-016-1498-2>.
- [55] H. Peng, Z. Mo, S. Liao, H. Liang, L. Yang, F. Luo, H. Song, Y. Zhong, B. Zhang, High Performance Fe- and N- Doped Carbon Catalyst with Graphene Structure for Oxygen Reduction, *Sci Rep.* 3 (2013) 1765. <https://doi.org/10.1038/srep01765>.
- [56] X. Xu, C. Shi, Q. Li, R. Chen, T. Chen, Fe–N-Doped carbon foam nanosheets with embedded Fe₂O₃ nanoparticles for highly efficient oxygen reduction in both alkaline and acidic media, *RSC Adv.* 7 (2017) 14382–14388. <https://doi.org/10.1039/C6RA27826D>.
- [57] D. Yan, Y. Li, J. Huo, R. Chen, L. Dai, S. Wang, Defect Chemistry of Nonprecious-Metal Electrocatalysts for Oxygen Reactions, *Advanced Materials.* 29 (2017) 1606459. <https://doi.org/10.1002/adma.201606459>.
- [58] X. Yan, Y. Jia, X. Yao, Defects on carbons for electrocatalytic oxygen reduction, *Chem. Soc. Rev.* 47 (2018) 7628–7658. <https://doi.org/10.1039/C7CS00690J>.
- [59] E. Groppo, F. Bonino, F. Cesano, A. Damin, M. Manzoli, CHAPTER 4: Raman, IR and INS Characterization of Functionalized Carbon Materials, in: *Metal-Free Functionalized Carbons in Catalysis*, 2018: pp. 103–137. <https://doi.org/10.1039/9781788013116-00103>.
- [60] K. Aoudia, S. Azem, N. Aït Hocine, M. Gratton, V. Pettarin, S. Seghar, Recycling of waste tire rubber: Microwave devulcanization and incorporation in a thermoset resin, *Waste Management.* 60 (2017) 471–481. <https://doi.org/10.1016/j.wasman.2016.10.051>.
- [61] Y. Guo, D.A. Rockstraw, Activated carbons prepared from rice hull by one-step phosphoric acid activation, *Microporous and Mesoporous Materials.* 100 (2007) 12–19. <https://doi.org/10.1016/j.micromeso.2006.10.006>.
- [62] W. Yang, Z. Du, Z. Ma, G. Wang, H. bai, G. Shao, Facile synthesis of nitrogen-doped hierarchical porous lamellar carbon for high-performance supercapacitors, *RSC Adv.* 6 (2015). <https://doi.org/10.1039/C5RA21431A>.
- [63] Y. Liu, J. Li, W. Li, Y. Li, F. Zhan, H. Tang, Q. Chen, Exploring the nitrogen species of nitrogen doped graphene as electrocatalysts for oxygen reduction reaction in Al–air batteries, *International Journal of Hydrogen Energy.* 41 (2016) 10354–10365. <https://doi.org/10.1016/j.ijhydene.2015.10.109>.

- [64] Y.V. Fedoseeva, E.V. Lobiak, E.V. Shlyakhova, K.A. Kovalenko, V.R. Kuznetsova, A.A. Vorfolomeeva, M.A. Grebenkina, A.D. Nishchakova, A.A. Makarova, L.G. Bulusheva, A.V. Okotrub, Hydrothermal Activation of Porous Nitrogen-Doped Carbon Materials for Electrochemical Capacitors and Sodium-Ion Batteries, *Nanomaterials*. 10 (2020) 2163. <https://doi.org/10.3390/nano10112163>.
- [65] M.A. Costa de Oliveira, B. Mecheri, A. D'Epifanio, E. Placidi, F. Arciprete, F. Valentini, A. Perandini, V. Valentini, S. Licoccia, Graphene oxide nanoplateforms to enhance catalytic performance of iron phthalocyanine for oxygen reduction reaction in bioelectrochemical systems, *Journal of Power Sources*. 356 (2017) 381–388. <https://doi.org/10.1016/j.jpowsour.2017.02.009>.
- [66] G. Lota, P. Krawczyk, K. Lota, A. Sierczyńska, Ł. Kolanowski, M. Baraniak, T. Buchwald, The application of activated carbon modified by ozone treatment for energy storage, *J Solid State Electrochem*. 20 (2016) 2857–2864. <https://doi.org/10.1007/s10008-016-3293-5>.
- [67] H. Hadoun, Z. Sadaoui, N. Souami, D. Sahel, I. Toumert, Characterization of mesoporous carbon prepared from date stems by H₃PO₄ chemical activation, *Applied Surface Science*. 280 (2013) 1–7. <https://doi.org/10.1016/j.apsusc.2013.04.054>.
- [68] X. Liu, L. Jiang, Z. Zhu, S. Chen, Y. Dou, P. Liu, Y. Wang, H. Yin, Z. Tang, H. Zhao, Wet-chemistry grafted active pyridinic nitrogen sites on holey graphene edges as high performance ORR electrocatalyst for Zn-Air batteries, *Materials Today Energy*. 11 (2019) 24–29. <https://doi.org/10.1016/j.mtener.2018.10.010>.
- [69] S. Kabir, K. Artyushkova, A. Serov, B. Kiefer, P. Atanassov, Binding energy shifts for nitrogen-containing graphene-based electrocatalysts – experiments and DFT calculations, *Surface and Interface Analysis*. 48 (2016) 293–300. <https://doi.org/10.1002/sia.5935>.
- [70] R. Gokhale, Y. Chen, A. Serov, K. Artyushkova, P. Atanassov, Direct synthesis of platinum group metal-free Fe-N-C catalyst for oxygen reduction reaction in alkaline media, *Electrochemistry Communications*. 72 (2016) 140–143. <https://doi.org/10.1016/j.elecom.2016.09.013>.
- [71] T. Kato, Y. Yamada, Y. Nishikawa, T. Otomo, H. Sato, S. Sato, Origins of peaks of graphitic and pyrrolic nitrogen in N1s X-ray photoelectron spectra of carbon materials: quaternary nitrogen, tertiary amine, or secondary amine?, *J Mater Sci*. 56 (2021) 15798–15811. <https://doi.org/10.1007/s10853-021-06283-5>.

- [72] M.M. Hossen, K. Artyushkova, P. Atanassov, A. Serov, Synthesis and characterization of high performing Fe-N-C catalyst for oxygen reduction reaction (ORR) in Alkaline Exchange Membrane Fuel Cells, *Journal of Power Sources*. 375 (2018) 214–221. <https://doi.org/10.1016/j.jpowsour.2017.08.036>.
- [73] C. Santoro, S. Rojas-Carbonell, R. Awais, R. Gokhale, M. Kodali, A. Serov, K. Artyushkova, P. Atanassov, Influence of platinum group metal-free catalyst synthesis on microbial fuel cell performance, *Journal of Power Sources*. 375 (2018) 11–20. <https://doi.org/10.1016/j.jpowsour.2017.11.039>.
- [74] N. Ramaswamy, S. Mukerjee, Fundamental Mechanistic Understanding of Electrocatalysis of Oxygen Reduction on Pt and Non-Pt Surfaces: Acid versus Alkaline Media, *Advances in Physical Chemistry*. 2012 (2012) e491604. <https://doi.org/10.1155/2012/491604>.
- [75] W. Zhong, Z. Wang, S. Han, L. Deng, J. Yu, Y. Lin, X. Long, M. Gu, S. Yang, Identifying the Active Sites of a Single Atom Catalyst with pH-Universal Oxygen Reduction Reaction Activity, *Cell Reports Physical Science*. 1 (2020) 100115. <https://doi.org/10.1016/j.xcrp.2020.100115>.
- [76] C. Santoro, P. Bollella, B. Erable, P. Atanassov, D. Pant, Oxygen reduction reaction electrocatalysis in neutral media for bioelectrochemical systems, *Nat Catal*. 5 (2022) 473–484. <https://doi.org/10.1038/s41929-022-00787-2>.
- [77] X. Ge, A. Sumboja, D. Wu, T. An, B. Li, F.W.T. Goh, T.S.A. Hor, Y. Zong, Z. Liu, Oxygen Reduction in Alkaline Media: From Mechanisms to Recent Advances of Catalysts, *ACS Catal*. 5 (2015) 4643–4667. <https://doi.org/10.1021/acscatal.5b00524>.
- [78] S. Rojas-Carbonell, C. Santoro, A. Serov, P. Atanassov, Transition metal-nitrogen-carbon catalysts for oxygen reduction reaction in neutral electrolyte, *Electrochemistry Communications*. 75 (2017) 38–42. <https://doi.org/10.1016/j.elecom.2016.12.011>.
- [79] A. Bonakdarpour, M. Iefèvre, R. Yang, F. Jaouen, T. Dahn, J.-P. Dodelet, J. Dahn, Impact of Loading in RRDE Experiments on Fe-N-C Catalysts: Two- or Four-Electron Oxygen Reduction?, *Electrochemical and Solid State Letters*. 11 (2008) B105–B108. <https://doi.org/10.1149/1.2904768>.
- [80] B.K. Mutuma, N.F. Sylla, A. Bubu, N.M. Ndiaye, C. Santoro, A. Brilloni, F. Poli, N. Manyala, F. Soavi, Valorization of biodigester plant waste in electrodes for supercapacitors

- and microbial fuel cells, *Electrochimica Acta*. 391 (2021) 138960.
<https://doi.org/10.1016/j.electacta.2021.138960>.
- [81] C. Santoro, A. Serov, C.W.N. Villarrubia, S. Stariha, S. Babanova, K. Artyushkova, A.J. Schuler, P. Atanassov, High catalytic activity and pollutants resistivity using Fe-AAPyr cathode catalyst for microbial fuel cell application, *Sci Rep*. 5 (2015) 16596.
<https://doi.org/10.1038/srep16596>.
- [82] C. Santoro, C. Arbizzani, B. Erable, I. Ieropoulos, Microbial fuel cells: From fundamentals to applications. A review, *Journal of Power Sources*. 356 (2017) 225–244.
<https://doi.org/10.1016/j.jpowsour.2017.03.109>.
- [83] C. Santoro, M. Kodali, S. Herrera, A. Serov, I. Ieropoulos, P. Atanassov, Power generation in microbial fuel cells using platinum group metal-free cathode catalyst: Effect of the catalyst loading on performance and costs, *Journal of Power Sources*. 378 (2018) 169–175.
<https://doi.org/10.1016/j.jpowsour.2017.12.017>.
- [84] C. Santoro, M.R. Talarposhti, M. Kodali, R. Gokhale, A. Serov, I. Merino-Jimenez, I. Ieropoulos, P. Atanassov, Microbial Desalination Cells with Efficient Platinum-Group-Metal-Free Cathode Catalysts, *ChemElectroChem*. 4 (2017) 3322–3330.
<https://doi.org/10.1002/celec.201700626>.
- [85] S. Brocato, A. Serov, P. Atanassov, pH dependence of catalytic activity for ORR of the non-PGM catalyst derived from heat-treated Fe–phenanthroline, *Electrochimica Acta*. 87 (2013) 361–365. <https://doi.org/10.1016/j.electacta.2012.09.053>.
- [86] M. Muhyuddin, N. Zocche, R. Lorenzi, C. Ferrara, F. Poli, F. Soavi, C. Santoro, Valorization of the inedible pistachio shells into nanoscale transition metal and nitrogen codoped carbon-based electrocatalysts for hydrogen evolution reaction and oxygen reduction reaction, *Mater Renew Sustain Energy*. 11 (2022) 131–141. <https://doi.org/10.1007/s40243-022-00212-5>.
- [87] D. Singh, J. Tian, K. Mamtani, J. King, J.T. Miller, U.S. Ozkan, A comparison of N-containing carbon nanostructures (CNx) and N-coordinated iron–carbon catalysts (FeNC) for the oxygen reduction reaction in acidic media, *Journal of Catalysis*. 317 (2014) 30–43.
<https://doi.org/10.1016/j.jcat.2014.05.025>.
- [88] Y. Hu, J.O. Jensen, W. Zhang, L.N. Cleemann, W. Xing, N.J. Bjerrum, Q. Li, Hollow Spheres of Iron Carbide Nanoparticles Encased in Graphitic Layers as Oxygen Reduction Catalysts,

Angewandte Chemie International Edition. 53 (2014) 3675–3679.
<https://doi.org/10.1002/anie.201400358>.

[89] C.H. Choi, C. Baldizzone, J.-P. Grote, A.K. Schuppert, F. Jaouen, K.J.J. Mayrhofer, Stability of Fe-N-C Catalysts in Acidic Medium Studied by Operando Spectroscopy, *Angewandte Chemie International Edition*. 54 (2015) 12753–12757.
<https://doi.org/10.1002/anie.201504903>.

[90] Q. Ma, H. Jin, J. Zhu, Z. Li, H. Xu, B. Liu, Z. Zhang, J. Ma, S. Mu, Stabilizing Fe–N–C Catalysts as Model for Oxygen Reduction Reaction, *Advanced Science*. 8 (2021) 2102209.
<https://doi.org/10.1002/advs.202102209>.

[91] Y. He, G. Wu, PGM-Free Oxygen-Reduction Catalyst Development for Proton-Exchange Membrane Fuel Cells: Challenges, Solutions, and Promises, *Acc. Mater. Res.* 3 (2022) 224–236. <https://doi.org/10.1021/accountsmr.1c00226>.

[92] D. Banham, S. Ye, K. Pei, J. Ozaki, T. Kishimoto, Y. Imashiro, A review of the stability and durability of non-precious metal catalysts for the oxygen reduction reaction in proton exchange membrane fuel cells, *Journal of Power Sources*. 285 (2015) 334–348.
<https://doi.org/10.1016/j.jpowsour.2015.03.047>.